

Chapter 5

GaN and $\text{Al}_x\text{Ga}_{1-x}\text{N}$ on sapphire substrates

5.1 Introduction

Gallium-aluminium nitride alloys may be promising materials for optical applications, particularly light-emitting diodes based on InGaN/AlGaN heterostructures grown on sapphire substrate have achieved practical level¹⁾ and an electrically pumped III-V nitride lasers have also been reported.²⁻⁴⁾ The successful application of these materials in the fabrication of optoelectronic devices, encourages increasing work on the characterization of the fundamental properties of these materials. Usually, GaN grown on Al_2O_3 (0001) has a hexagonal wurtzite structure, and the optical axis (i.e., the hexagonal c axis) of the film is perpendicular to the substrate plane.⁵⁾ Therefore, GaN on sapphire is optically anisotropic with two independent refractive index constants, n_{\perp} ($E \perp c$) and n_{\parallel} ($E \parallel c$). The knowledge of this is critical in designing new optoelectronic devices. Suffice it to say that the recent development of the GaN laser diode would have been impossible without overcoming the difficulties with the production and maintenance of a crack-free GaN layer⁶⁾. Thus mechanical characteristics of GaN materials are also key parameters for its successful application.

The optical transmission, which is effective and accurate method to determine the optical constants below the fundamental absorption edge, has been used to study GaN by several authors.^{7,8)} The accuracy of refractive index n in the transmission method is mainly determined by the accuracy of thickness measurements.⁷⁾ Spectroscopic ellipsometry (SE) has

widely been used as a nondestructive technique to investigate the optical response of semiconductors. In particular, the film thickness can be determined very accurately by fitting SE data (Δ, Ψ) in the interference part of spectrum using a suitable model.⁹⁾ Adachi et al. also proposed that the overall precision in the index value was 0.02 using the three-phase model analysis for (Al_xGa_{1-x})_{0.5}In_{0.5}P quaternary alloys on GaAs in the interference part of spectrum.¹⁰⁾ And, the depth-sensing indentation technique provides complete information on the mechanical behaviors of solids studied. It has widely been used to investigate the hardness and the pressure-induced phase transformation of semiconductor materials.^{11,12)}

In this chapter, a method has been described to determine the optical constants of GaN grown on sapphire over the energy range of 0.78 - 4.77 eV by spectroscopic ellipsometry (SE) and optical transmission measurements. An excellent fitting of SE measurement data (Δ, Ψ) can be obtained using the Sellmeier dispersion equation, provided the fitted data set is limited to the interference part of the spectrum.

The method is proposed to determine the thickness and index n_{\perp} from the interference fringes of the polarized reflectance $|r_s|$ ($E \perp c$) at two incident angles, 65° and 75°, and index n_{\parallel} from the interference fringes of the polarized reflectance $|r_p|$ at an incident angle of 75°. The accuracy to which n_{\perp} , n_{\parallel} and thickness are determined, which depends on the accuracy of the incident angle measurements and is quite independent of the optical constants of the substrate and overlayer on the surface, is estimated to be better than $\pm 2\%$. An excellent agreement between the calculated results and measurement have been obtained.

It has been studied that the surface deformation of GaN film on sapphire by means of depth-sensing indentation experiments with the pointed diamond (Berkovich triangular pyramid) and 5 μm radius spherical-tipped diamond. We have found that the critical transition load for the onset of plastic deformation is dependent on the thickness of film. "true hardness" of GaN film on sapphire have been calculated, and compared with the results of InGaN films on sapphire.

The dielectric function of Al_xGa_{1-x}N below the fundamental band edge and assume a two layer model for samples of Al_xGa_{1-x}N/GaN/Sapphire have been described by sum of Sellmeier dispersion relationship and a free exciton. An excellent simultaneous fit of the

model to measured Ψ data of SE at three angles of incidence, 40°, 50° and 60° has been obtained.

5.2 Characterization for GaN film on sapphire substrate

5.2.1 The optical constants of GaN film on sapphire substrate

Experiment

Undoped GaN epitaxial layer was grown on one side polished sapphire (0001) substrate by metal-organic chemical-vapor deposition (MOCVD), using ammonia (NH₃) as the nitrogen source. The uncoated backside of the substrate was rough and was mirror polished before the optical transmission measurement. The SE measurement was carried out at an incident angle of 60° over 260 to 830 nm wavelength range, and optical transmission measurement over 370 to 1600 nm wavelength range. Both the measurements were performed at room temperature.

Results

The measured SE data, Δ and Ψ , of the GaN film in the interference part of spectrum are shown in Fig. 5.1 (dotted lines). We analyze these experimental data using a Sellmeir-type dispersion relationship¹³⁾

$$\begin{aligned} n^2(\lambda) &= A_0^2 + \frac{A_1^2}{\lambda^2 - A_2^2} \\ k(\lambda) &= 0, \end{aligned} \quad (5.1)$$

where A_0 , A_1 and A_2 are the fitting parameters and λ is the wavelength of light (in micrometers). The fitted Δ and Ψ spectra, simulated with the best-fit model parameters which are summarized in Table 5.1, are shown by solid lines in Fig. 5.1. The thickness (1.25 μm) of GaN film matches closely with that obtained by SEM cross-sectional thickness measurement (1.3 μm). The fit was done by minimizing the mean square error d_2 (unbiased).¹⁴⁾ The excellent fit is found in the wavelength range larger than 400 nm, and the deviations of

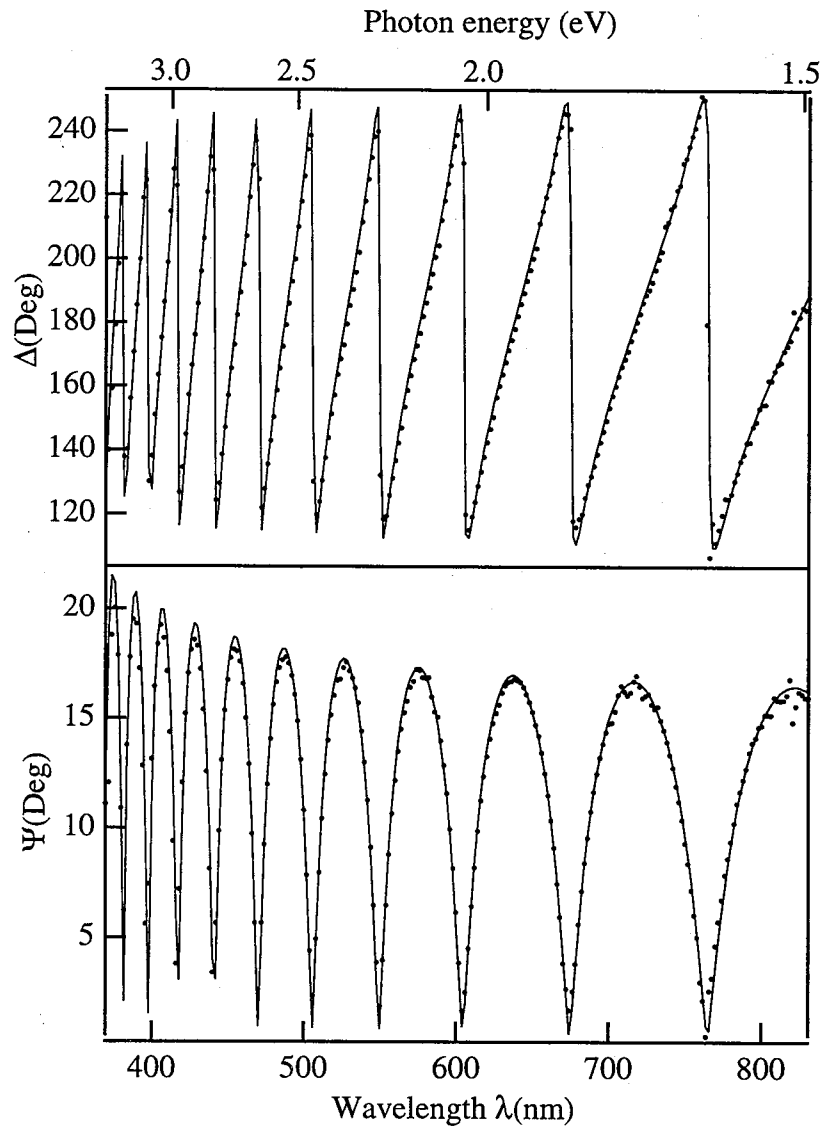


Figure 5.1: Measured (dotted line) and calculated (solid line) Δ and Ψ spectra of GaN on sapphire substrate in the interference part of the spectrum.

the fit from the experimental data above 3.4 eV are due to the absorption of light because of the interband transitions.

An optical transmission spectrum of the same sample is shown in Fig. 5.2. Transmission of the bare sapphire substrate, T_s , is also shown in the same figure as the dotted line, which is calculated by using the expression¹⁵⁾

$$T_s = \frac{2n_s}{n_s^2 - 1}, \quad (5.2)$$

where n_s is refractive index of sapphire, taken from the ref. 13. As can be seen from Fig. 5.2

Table 5.1: Best-fit parameters of GaN on a sapphire substrate determined by SE measurements. The 90% confidence limits are given with (\pm).

A_0	A_1 (nm^2)	A_2 (nm^2)	Thickness d (nm^2)	δ
2.27 ± 0.02	304.7 ± 7.8	294.0 ± 4.5	1250.2 ± 16	6.2

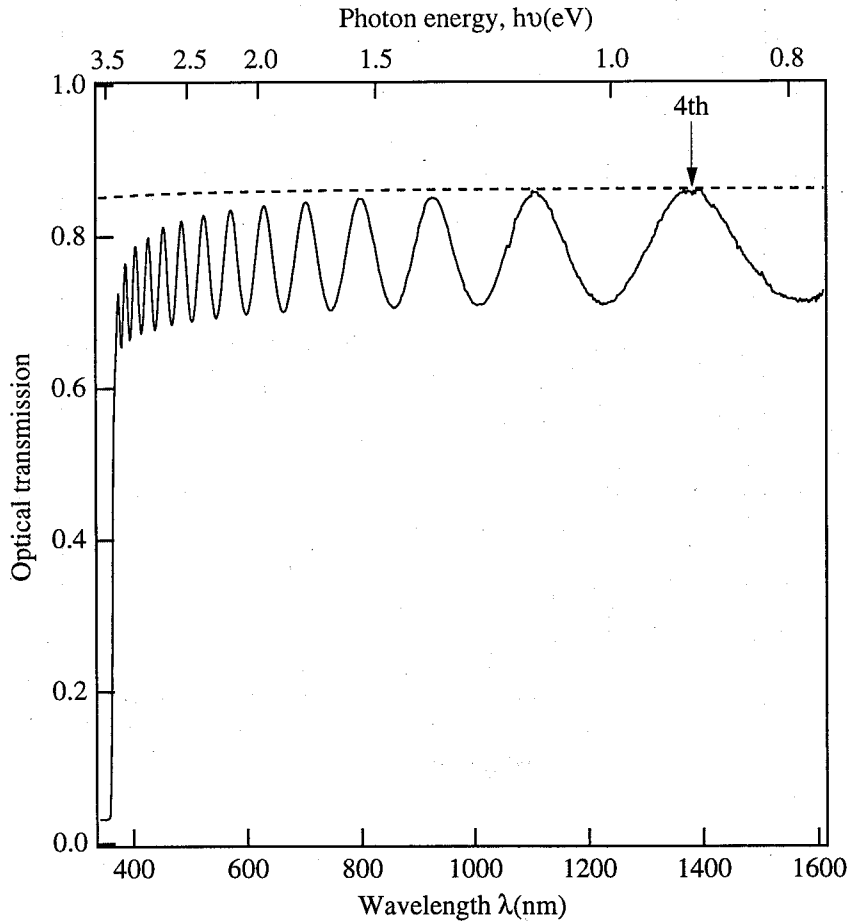


Figure 5.2: Optical transmission spectrum of GaN on sapphire substrate.

that the lowest energy maximum (4th order) of the interference fringes coincides with T_s . Two conclusions can be made from this; first, the absorption coefficient is zero near this wavelength region, second, the roughness of the surfaces on both sides of the sample can be ignored.

The film thickness, d , obtained by fitting to SE data, together with the order m of the interference fringes, is then used to obtain refined values of refractive indices from the

relationship¹⁵⁾

$$n = \frac{m\lambda}{2d}, \quad (5.3)$$

and are shown by the solid circles in Fig. 5.3. Using the same thickness of the film, refractive index spectrum of GaN has also been obtained from SE measurements and is shown in Fig. 5.3 by the solid line. For comparison, the refractive index spectrum of GaN, obtained from ref. 4, is also shown in Fig. 5.3 as a dashed line. The deviation between these two experimental data is about 2% at 1.0 eV. However, this deviation is within the experimental error of the transmission measurement (2%)⁴⁾ and SE.

Using the refractive indices obtained from transmission measurement and the thickness in Table 5.1, the absorption coefficient as a function of wavelength are calculated following the formula of the interference-free transmission (T_a) details of which are given in ref. 13. Fig. 5.3(b) shows the plot of absorption coefficient versus wavelength obtained by both the SE and transmission method. Absorption coefficient is much smaller than that given in ref. 8 in the energy range of 0.78 - 3.0 eV, indicated that the deep level at ~2.0 eV is not observed in our sample. The non-zero absorption coefficient below the fundamental band may be due to contribution from the deep level at near 1.0 eV. A free exciton characteristic structure is observed and is shown in the inset of Fig. 5.3(a). High-temperature free exciton luminescence in GaN has also been observed by photoluminescence and photoreflectance spectra.^{3,16)} A simple estimate of transition energy of the exciton based on the Lorentzian line-shape functional form is¹⁷⁾

$$\frac{d^2\varepsilon}{dE^2} = Ae^{i\phi}(E - E_0 + i\Gamma)^{-m} \quad (5.4)$$

where A and ϕ are the amplitude and phase of the line shape, respectively, and E_0 and Γ are the energy and empirical broadening parameter of the transition, respectively. Characteristic parameter m is equal to 2, and describes the nature of interband excitonic transition. From the numerical fitting of second derivative of the dielectric function ε with respect to photon energy using Eq. 5.4, we found exciton transition energy at room temperature to be 3.44 eV, in reasonable agreement with the reported result of 3.42 eV, obtained from modulated photoreflectance measurements and photoluminescence spectra.^{3,16)}

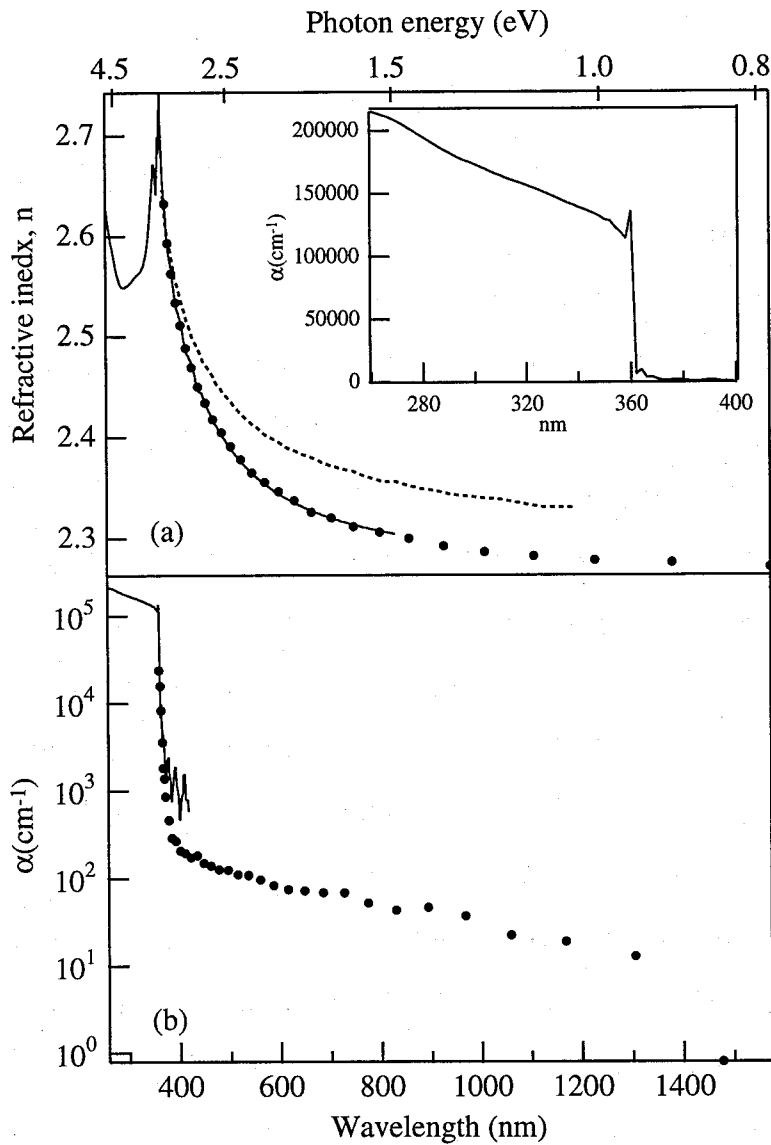


Figure 5.3: The optical constants of GaN on sapphire vs. wavelength. (a) the refractive indices determined from SE (solid line) and transmission (data points) compared with data from ref. 4. (b) the absorption coefficient determined from SE (solid line) and transmission (data points). The expanded figure of absorption coefficient obtained by SE is shown in the inset.

5.2.2 Optical anisotropy of GaN film on sapphire substrate

Experiment

An undoped GaN epitaxial layer was grown on a sapphire (0001) substrate by metal-organic chemical-vapor deposition (MOCVD), using ammonia (NH_3) as the nitrogen source (details will be published elsewhere). The sample did not contain a buffer layer. The

SE measurement was carried out at an angle of incidence of 70° over a 360 to 830 nm wavelength range, and polarized reflectance measurements ($|r_s|$ and $|r_p|$) were taken at angles of incidence of 65° and 75° over a 360 to 830 nm wavelength range. All of the measurements were performed at room temperature.

Results

Using the formulae according to ref. 18, the polarized reflection coefficients can be written as,

$$\begin{aligned} |r_j|^2 &= \frac{|r_1^j|^2 + 2r_1^j r_2^j \cos\beta_j + |r_2^j|^2}{1 + 2r_1^j r_2^j \cos\beta_j + |r_1^j|^2 |r_2^j|^2} \\ &= 1 - \frac{(1 - |r_1^j|^2)(1 - |r_2^j|^2)}{1 + 2r_1^j r_2^j \cos\beta_j + |r_1^j|^2 |r_2^j|^2} \\ j &= s, p, \end{aligned} \quad (5.5)$$

and here the phase difference β_j is given by

$$\beta_s = \frac{4\pi d (n_{\perp}^2 - \sin^2 \phi)^{1/2}}{\lambda}, \quad (5.6)$$

for s polarized light (the electric vector perpendicular to the plane of incidence), and

$$\beta_p = \frac{4\pi d n_{\perp} (n_{\parallel}^2 - \sin^2 \phi)^{1/2}}{\lambda n_{\parallel}}, \quad (5.7)$$

for p polarized light (the electric vector parallel to the plane of incidence). In Eq. 5.5, use has been made of the conditions, i.e. both the film and substrate are nonabsorbing materials ($k=0$) and the c-axis is perpendicular to the interface. The basic equation for interference fringes is

$$\beta_j = m\pi. \quad (5.8)$$

For $r_1^j r_2^j > 0$, m is an even integer for maxima and an odd integer for minima, and for $r_1^j r_2^j < 0$, m is an odd integer for maxima and an even integer for minima. It is clear from Eq. 5.6 and 5.7 that if $n_{\parallel} = n_{\perp}$, β_p is equal to β_s .

In Fig. 5.4, we plot $\beta_j \lambda / 4\pi$ as a function of wavelength for incidence angles of 65° and 75°. It is obvious that $\beta_p \lambda / 4\pi$ is larger than $\beta_s \lambda / 4\pi$ over the entire measured wavelength

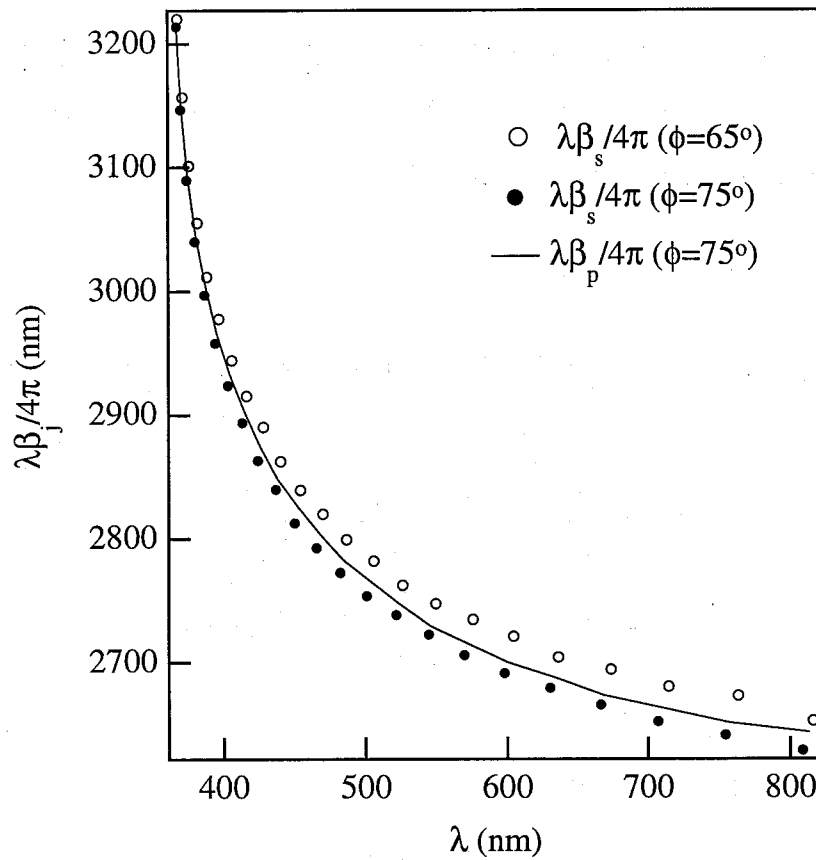


Figure 5.4: The phase difference, $\lambda\beta_j/4\pi$, determined from the wavelength of maxima and minima of the s and p polarized reflection spectra (ϕ , the incident angle).

range at an incidence angle of 75° . Therefore, it can be concluded that n_{\parallel} is larger than n_{\perp} over this wavelength range.

Using the interpolation of the cubic spline method, the average thickness \bar{d} of film from Eq. 5.6, at two incident angles, 65° and 75° , can be written as,

$$\bar{d} = \frac{1}{N} \sum_i^N \sqrt{\frac{\lambda_i (\beta_s^2(\lambda_i, 65^\circ) - \beta_s^2(\lambda_i, 75^\circ))}{4\pi (\sin^2 75^\circ - \sin^2 65^\circ)}}. \quad (5.9)$$

This yielded $\bar{d} = 1241.6 \pm 42$ nm for our sample of GaN film on sapphire, which is in good agreement with the result of our SEM cross-sectional thickness measurement ($1.3 \mu\text{m}$). Once the thickness \bar{d} of the film is determined, the indices n_{\perp} and n_{\parallel} can be obtained using eqs. 5.6 and 5.7, and the results are shown in Fig. 5.5. The refractive index spectrum of GaN, obtained from ref. 19, is also shown in Fig. 5.5 (dashed line) for comparison. The

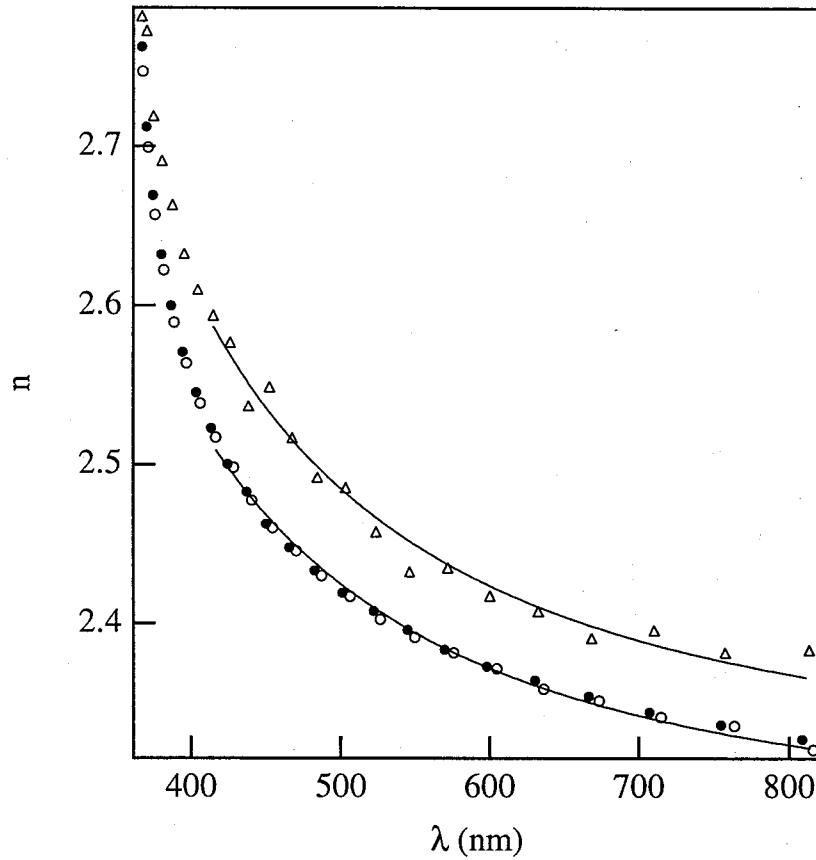


Figure 5.5: The refractive indices n_{\perp} (\circ, \bullet), taken from the incident angle 65° and 75° , respectively, and n_{\parallel} (Δ), taken from the incident angle 75° , determined from the phase difference, $\lambda\beta_j/4\pi$, and the thickness of the film (ϕ , the incident angle). The solid lines are the fit to a Sellmeier-type dispersion relationship $n^2(\lambda)=1+A\lambda^2/(\lambda^2-B)$. The dashed line represents the refractive index of $E \perp c$ for GaN on sapphire taken from ref. 19.

deviation between these two experimental data is about 1% at a wavelength of 600 nm. This deviation is within the experimental error of SE. Over the entire wavelength of measurement, the largest difference $(n_{\parallel}-n_{\perp})/n_{\perp}$ in the refractive indices for $E \perp c$ and $E \parallel c$ is 3%. It is important to estimate the high-frequency dielectric constant, ϵ_{∞} . Let us fit the experimental data of both the n_{\perp} and n_{\parallel} using a simple theoretical model, i.e. the first-order Sellmeier equation:^{20, 21)}

$$n^2(\lambda) = 1 + \frac{A\lambda^2}{\lambda^2 - B}, \quad (5.10)$$

where A and B are the fitting parameters and λ is the wavelength of light (in micrometers). The parameters obtained by fitting are as follows: $A=4.14$ and $B=0.038 \text{ mm}^2$ for $E \perp c$,

and $A=4.31$ and $B=0.034 \text{ nm}^2$ for $E \parallel c$. The value, $\epsilon_\infty=1+A (\lambda \rightarrow \infty)$, is a good approximation for ϵ_∞ in this one-oscillator model.^{20, 22)} The values we obtained for ϵ_∞ are 5.14 for $E \perp c$ and 5.31 for $E \parallel c$. These values are larger than those given in ref. 5 (4.5), and closer to the direct experimental observations (5.35).^{23, 24)}

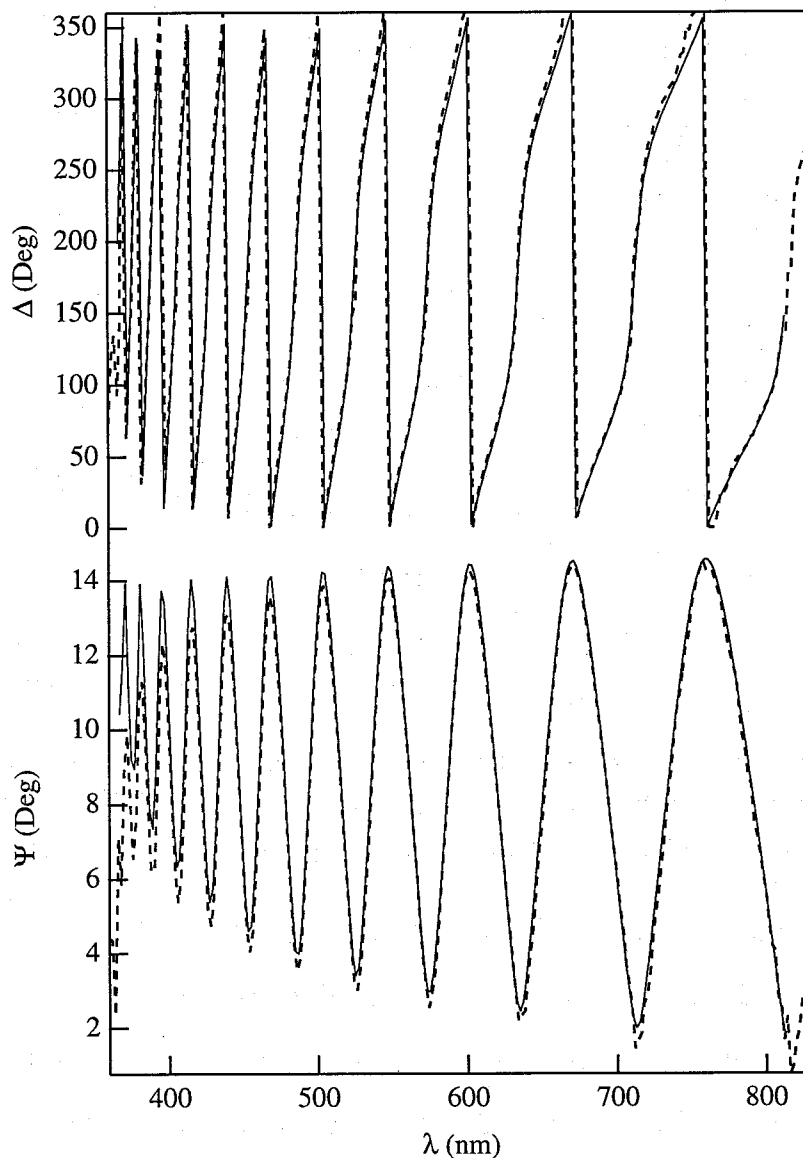


Figure 5.6: Calculated spectrum (solid lines) of the spectroscopic ellipsometry parameters, Δ and Ψ , using the results of n_\perp , n_\parallel and thickness of the film determined from the polarized reflection spectrum. The dashed lines indicate the corresponding experimental spectrum at an angle of incidence of 70° .

Figure 5.6 shows the numerically calculated spectrum of SE data Δ and Ψ (solid line), using results of the n_\perp , n_\parallel and thickness at an angle of incidence of 70° . The details of

the calculation procedure of ellipsometry angle Δ and Ψ for uniaxial anisotropic media is given in ref. 18. The dashed line is the measured data obtained by SE at the same incident angle. It is evident that the theoretically calculated data agree excellently well with the experimental data in wavelength ranges above 400 nm, and that the deviations of the calculated data from the experimental data below 400 nm is due to the non-zero absorption coefficient.

5.2.3 The mechanical constants and “ture hardness” of GaN films on sapphire substrate

Experiment

Undoped GaN epitaxial layers were grown on sapphire (0001) substrate by metal-organic chemical-vapor deposition (MOCVD), using ammonia (NH₃) as the nitrogen source. The thicknesses of GaN films studied are between 1.3 μm and 2.4 μm . The thickness of films were determined by means of spectroscopic ellipsometry (SE) and high resolution scanning electron microscopy (SEM) method. Indentation experiments were performed using the ultra-micro-indentation system UMIS-2000 equipped with a triangular sharp diamond indenter (Berkovich type) under higher ($P_{max}=500, 400, 300, 200, 100, 50$ and 20 mN) and lower ($P_{max}=10, 9, 8, 7, 6, 5$ and 4 mN) maximum indentation loads, and using alternating load-partial unload model with spherically tipped diamond indenter of 5 μm radius of 50 mN maximum indentation loads. All of the measurements were performed at room temperature.

Results and Discussion

In Fig. 5.7 we show the typical examples of the indentation hysteresis loops registered under higher ($P_{max}=500, 400, 300, 200, 100, 50$ and 20 mN) (a) and lower ($P_{max}=10, 9, 8, 7, 6, 5$ and 4 mN) (b) maximum indentation loads for the undoped GaN film grown by the MOCVD on sapphire substrate with a film thickness of 1.3 μm . In the loading-cycle parts, there obviously appears a pop-in (P), which corresponds to occurrence of dislocation loop nucleation, as observed for sapphire, but not for InGaN.¹¹⁾

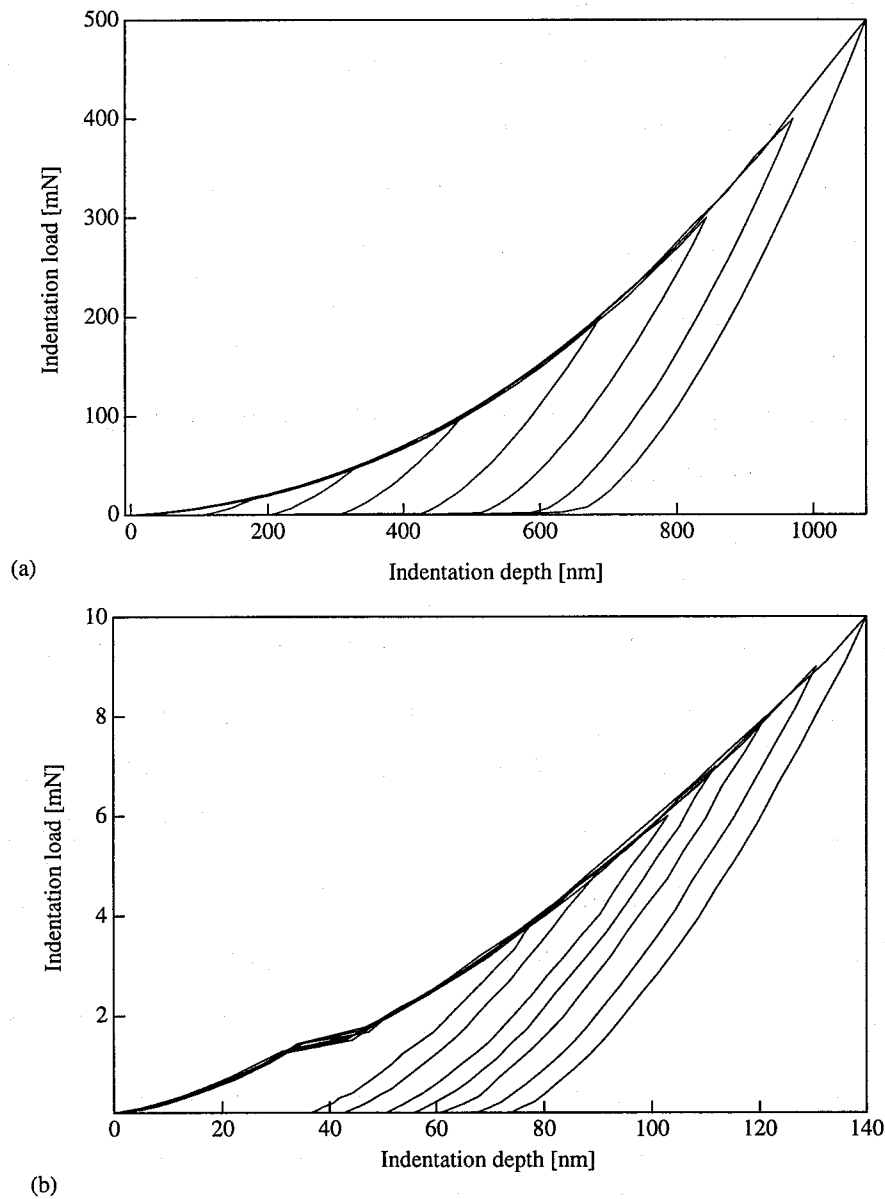


Figure 5.7: The indentation hysteresis loops obtained for undoped GaN on sapphire substrate under (a) higher and (b) lower maximum indentation loads.

It is worth noting that the critical load force (P_{crit}), at which the pop-in occurs, presents the significant differences for samples with different thicknesses of film. The value of P_{crit} appears to be greater for the thicker films. We suspect this phenomenon to be associated with differences of the crystal quality on the surface of the film, because in usual case with increasing thickness, the crystal quality on the surface of the film will be greatly improved. We found a similar behavior for GaAs films grown on Si by MOCVD.

In order to estimate the maximum shear stress existing beneath the loaded indenter at

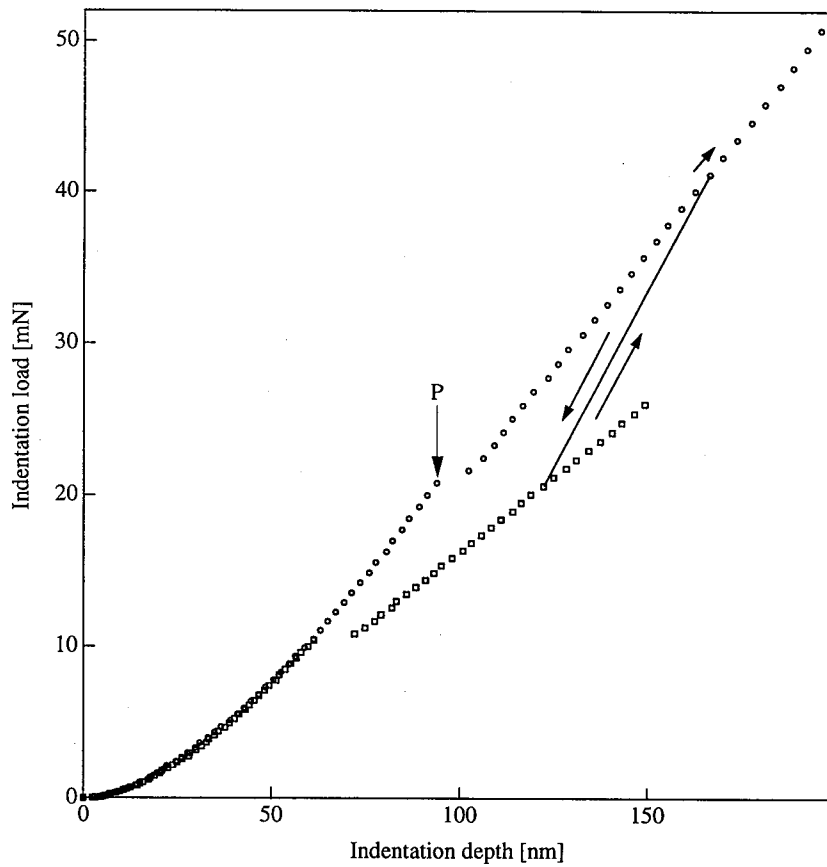


Figure 5.8: Schematic load-partial unload procedure to investigate the elastic-plastic response of GaN on sapphire with a spherical indenter of 5 μm radius.

the occurrence of the displacement discontinuity, we used the spherically tipped diamond indenter of 5 μm radius, beneath which the stress distribution is found to be more “well-behaved” than beneath a nominally pointed indenter.²⁵⁾ An alternating load-partial unload-displacement curve for sample with 1.3 μm film thickness is shown in Fig. 5.8. Below the critical load P_{crit} indentation response of the samples exhibits wholly elastic behavior, and average critical load P_{crit} , at which pop-in occurred, is about 21.0 ± 2 mN for 29 indentation test. The elastic analysis for the spherical case leads to the following relationship between the load, P , and the indenter displacement, h :²⁶⁾

$$h^{3/2} = (9/16)^{1/2} \frac{P}{E_{eff} R^{1/2}} \quad (5.11)$$

where E_{eff} is the effective composite elastic modulus and R the radius of curvature of the indenter. A plot of $h^{3/2}$ versus P thus will be a straight line whose slope, S , can be used to

find the effective value E_{eff} from

$$E_{eff} = (9/16)^{1/2} \frac{1}{SR^{1/2}} \quad (5.12)$$

The value of E_{eff} is 244 GPa and 237 GPa for samples with 1.3 μm and 2.4 μm film thicknesses, respectively. The difference between the above two values is about 2.9%, which is within the experimental error. Therefore, the thickness of GaN epilayer has no influence on the results presented in this study. The effective modulus value (E_{eff}) for each indenter/substrate combination can be calculated by

$$E_{eff} = \left[\frac{1 - \nu_i^2}{E_i} + \frac{1 - \nu_s^2}{E_s} \right]^{-1} \quad (5.13)$$

where the subscripts i and s refer to the indenter and material measured, respectively, E is Young's modulus, and ν is Poisson's ratio. For diamond²⁸, $E_i=1000$ GPa, $\nu_i=0.25$ are used and because of lack of Poisson's ratio and elastic constants for GaN, we have used the Poisson's ratio of AlN (0.287)²⁷ for the calculation. Thus calculated Young's modulus for GaN is found 290 GPa, which is very close to that of AlN (283 GPa).²⁷

The maximum shear stress occurring in the film at the critical load P_{crit} is given by:²⁸

$$\tau_{max} = 0.12 \left(\frac{P_{crit} E_s^2}{R^2} \right)^{1/3} \quad (5.14)$$

In this way, the maximum shear stress has been calculated for the two samples with

Table 5.2: The maximum shear stress values occurring at the critical load P_{crit} .

Material	E (GPa)	τ_{max} (GPa)	E/τ_{max}
GaN (2.4 μm)	290	5.4	~ 53
GaN (1.3 μm)	290	4.6	~ 63
Al ₂ O ₃ (0001)	390	8.5	~ 46

different thicknesses of GaN films and is shown in Table 5.2. The maximum shear stress of sample with 2.4 μm film thickness is obviously larger than that of sample with 1.3 μm film thickness.

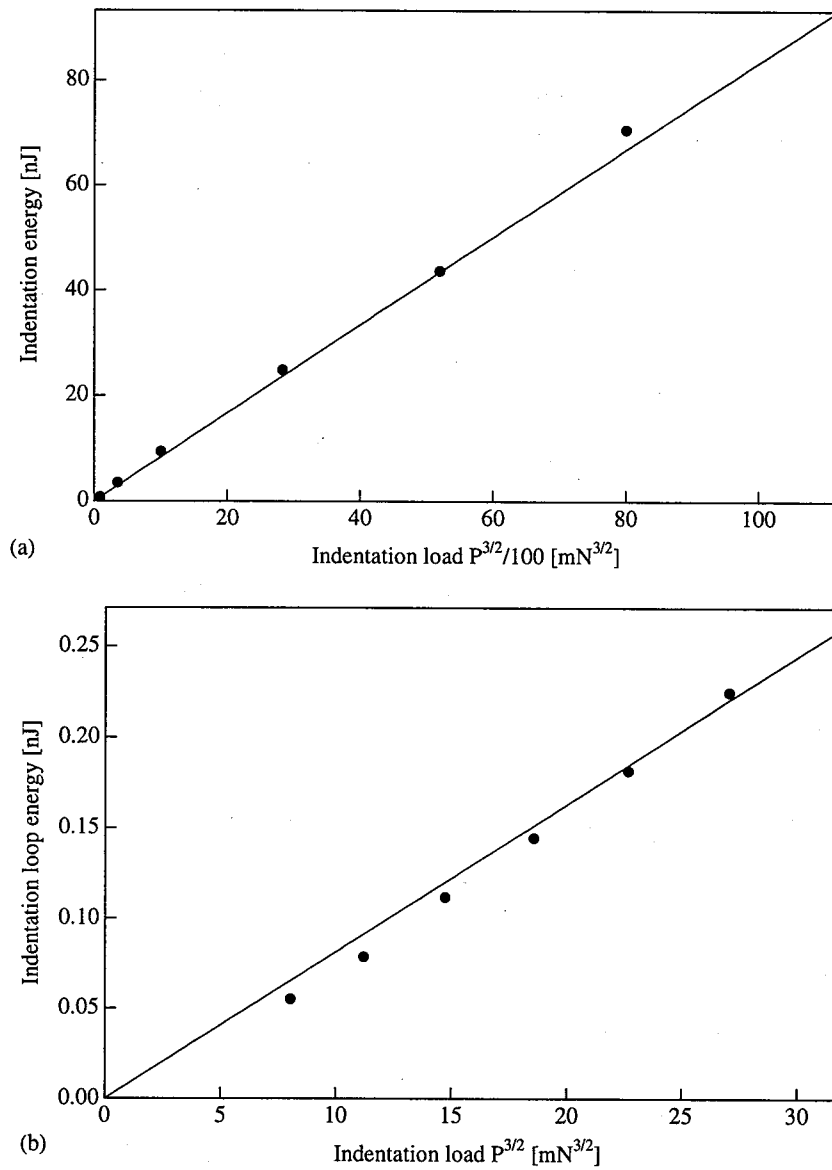


Figure 5.9: The relationship between the indentation loop energy U_r and the maximum indentation load ($U_r \rightarrow P_{max}^{3/2}$) for GaN under (a) higher and (b) lower maximum indentation loads.

The linear relationship between the indentation loop energy (U_r) and the applied maximum indentation load (P_{max}) has been used to calculate “true hardness”,²⁹⁾

$$U_r = \frac{1}{3} \sqrt{\frac{1}{\alpha_0 \tan^2 \psi}} \frac{1}{H} P_{max}^{3/2} \quad (5.15)$$

where α_0 and ψ are the geometrical constant and the semiapex angle of the indenter, respectively. The data from Figs. 5.7(a) and 5.7(b) have been replotted in this way, as shown in Figs. 5.9(a) and 5.9(b). The data of indentation loop energy (U_r) versus maximum

Table 5.3: The “true hardness” value of the GaN, InGaN and sapphire crystal measured by higher-load ($20 \text{ mN} < P_{max} < 500 \text{ mN}$) and lower-load ($2 \text{ mN} < P_{max} < 10 \text{ mN}$) indentation experiments and calculated according to Eq. 5 ($\alpha_0 = 3^{3/2}$ and $\psi = 67.3^\circ$ for the triangular tip indenter).

Material	True hardness (GPa)	True hardness (GPa)
	($20 \text{ mN} < P_{max} < 500 \text{ mN}$)	($2 \text{ mN} < P_{max} < 10 \text{ mN}$)
undoped GaN	53.6	56.3
undoped InGaN	52.0 ^a	-
sapphire	81.6 ^a	-

^a taken from ref. 11

indentation load (P_{max}) show reasonable fits to straight lines. The results for the hardness of GaN, together with that of In_{0.1}Ga_{0.9}N grown on sapphire and bulk sapphire, are listed in Table 5.3. It is found that the hardness of GaN is larger than that of In_{0.1}Ga_{0.9}N.

5.3 The optical properties of Al_xGa_{1-x}N/GaN heterostructure on sapphire

Experiment

Al_xGa_{1-x}N/GaN single heterostructure were grown on 2-inch-sapphire (0001) substrate using the horizontal atmospheric pressure metal-organic chemical-vapor deposition (MO CVD) method. Trimethylgallium (TMG), trimethylaluminum (TMA) and ammonia (NH₃) were used as source materials. The sapphire substrate was first heated at 1100°C for 10 min in a stream of hydrogen followed by the deposition of 30-nm-thick GaN as the buffer layer at 530°C. Then, a GaN layer with thickness of about 1.5 μm and an Al_xGa_{1-x}N layer with thickness in the range of 0.2-0.5 μm were grown at a fixed temperature of 1050°C. The molar fractions of AlN were determined by electron probe micro analysis (EPMA) and the thicknesses of the films were determined by both high resolution scanning electron microscopy (SEM) and spectroscopic ellipsometry (SE). The automatic ellipsometry used was of the rotating analyzer type. The 75 W xenon lamp was used as the light source, and the SE measurements were carried out in air over 360 to 830 nm wavelength range with a

step of 2 nm at three angles of incidence, 40°, 50° and 60°. Details concerning the structure of three samples studied are listed in Table 5.4.

In above section it was found that the refractive index of GaN below the fundamental band gap energy can be adequately described by Sellmeier dispersion equation and also we observed a clear free exciton absorption in high-quality GaN sample was also made at room temperature. So, in order to describe the dielectric function of Al_xGa_{1-x}N more accurately, the sum of Sellmeier dispersion equation and the exciton expression has been used to fit the SE data, which can be expressed by the following equation,

$$\varepsilon(\omega) = A + \frac{B\omega^2}{\omega_a^2 - \omega^2} + \frac{4\pi\alpha_e\omega_e^2}{\omega_e^2 - \left(\frac{\hbar^2 k^2}{m^*}\right)\omega_e - \omega^2 - i\Gamma_e\omega} \quad (5.16)$$

Here, the first two terms together are called the first-order Sellmeier dispersion equation¹³⁾ and the third term is the contribution from the exciton, which have been used to analyze the exciton of GaN in reflection spectra by M. Tchoukeu et al.¹⁶⁾ ω_e is the transverse frequency related to the exciton with an effective mass m^* , $4\pi\alpha_e\omega_e^2$ is the polarizability of the exciton resonance at $\omega=0$ and $k=0$, and Γ_e is the damping parameter used to account for the interactions of the exciton with the phonons and extrinsic defects. It can be mentioned here that the SE parameter Ψ is not sensitive to the presence of overlayer on the surface, such as oxide and rough layer, and therefore the comparison between the model and the experiment is made on the Ψ curve only in order to ignore the effect of such overlayers in the fitting.³⁰⁾ In addition, simultaneous fit to the spectra of Ψ , measured at three angles of incidence (40°, 50° and 60°.) are carried out to further increase the reliability of the parameters obtained by fitting, and the root-mean-square (rms) fractional error σ , defined by

$$\sigma^2 = \frac{1}{3} \left[\frac{\sum_j^n \left\{ \left(\Psi_j^{\text{exp}} - \Psi_j^{\text{cal}} \right)_{iang=40} \right\}^2}{\frac{1}{n} \sum_j^n \left\{ \left(\Psi_j^{\text{exp}} \right)_{iang=40} \right\}^2} + \frac{\sum_j^n \left\{ \left(\Psi_j^{\text{exp}} - \Psi_j^{\text{cal}} \right)_{iang=50} \right\}^2}{\frac{1}{n} \sum_j^n \left\{ \left(\Psi_j^{\text{exp}} \right)_{iang=50} \right\}^2} + \frac{\sum_j^n \left\{ \left(\Psi_j^{\text{exp}} - \Psi_j^{\text{cal}} \right)_{iang=60} \right\}^2}{\frac{1}{n} \sum_j^n \left\{ \left(\Psi_j^{\text{exp}} \right)_{iang=60} \right\}^2} \right] \quad (5.17)$$

has been used as judgment of the quality of the fit between the measured and calculated data, which has also been used by C. C. Kim et al.³¹⁾ in simultaneous fits to dielectric function $\varepsilon(\omega)$ and its derivatives with respect to energy for GaAs.

Table 5.4: Best fit parameters of Al_xGa_{1-x}N/GaN on sapphire substrate determined by SE measurements and SEM thicknesses measurements.

Sample No.	structure	d ₁ (μm)		d ₂ (μm)		Exciton Energy (eV)	Braodening (meV)	σ
		SE	SEM	SE	SEM			
1	GaN/Sapphire	0	/	1.396	/	3.44	35	0.167
2	Al _{0.087} Ga _{0.913} N/GaN/Sapphire	0.225	0.2	1.532	1.5	3.73	22	0.159
3	Al _{0.151} Ga _{0.849} N/GaN/Sapphire	0.310	0.3	1.552	1.5	3.95	78	0.232

We first attempt to fit the data of sample 1 using the above-mentioned method, assuming a three-phase (ambient/GaN/Sapphire) model. The refractive index function of sapphire was taken from ref. 13. The calculated Ψ spectrum for sample 1 is shown in Fig. 5.10 by solid line, and the parameters obtained are shown in Table 5.4. An excellent agreement between the measured and calculated spectra has been obtained as can be seen from Fig. 5.10. The refractive index function of sample 1 in the wavelength range of 300 - 830 nm, along with the refractive index of GaN taken from the previous report, is shown in Fig. 5.11. It is obvious that there is no appreciable difference between the two results at whole wavelength range measured. It can be noted here that for all samples the refractive index n and extinction coefficient k in the wavelength region above the bandgap are obtained by assuming a two-phase (such as, ambient/GaN) model. This assumption of two-phase model is justified by two reasons. First, the penetration depth of light from the surface is about 100 nm in the wavelength range above bandgap. Since, the top layers for all the samples are thicker than 100 nm, the effect of bottom layer and/or substrate is negligible in the above wavelength region. Second, not considering the overlayers on the surface does not deteriorate the fitting of SE spectra, Δ , below the fundamental band edge. Therefore, it is reasonable to estimate

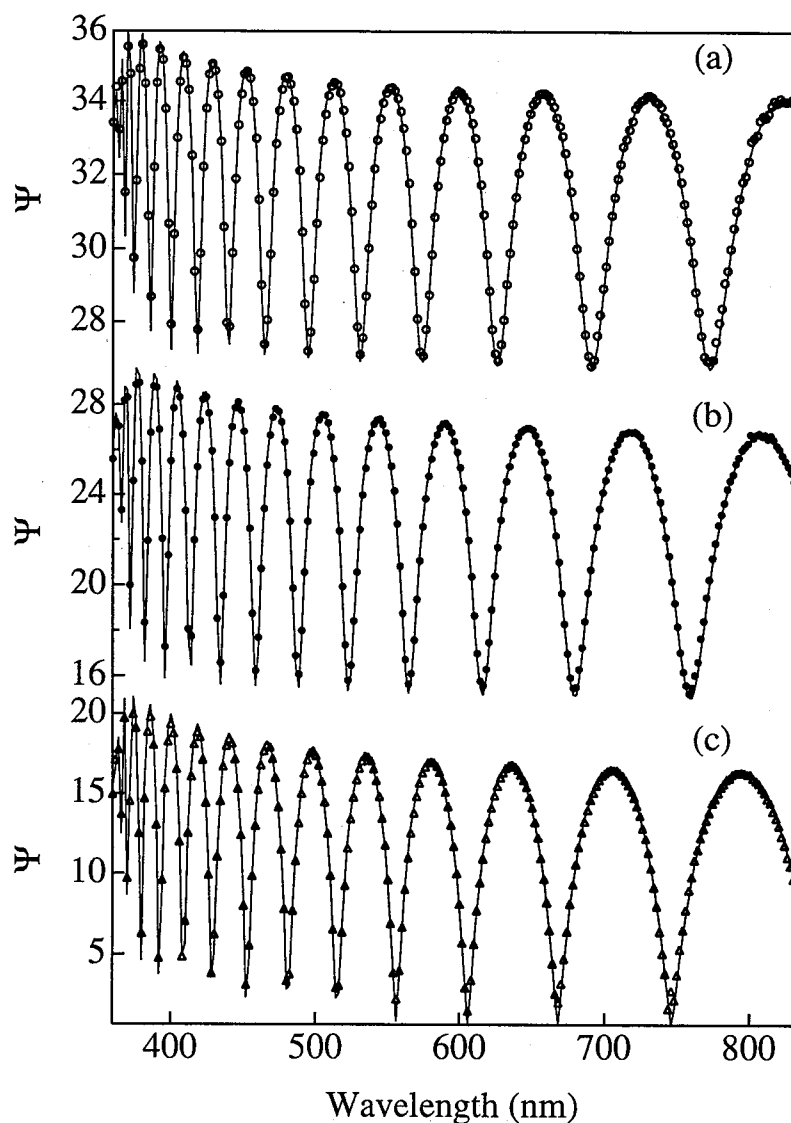


Figure 5.10: Measured (dotted line) and calculated (solid line) Ψ spectra of sample 1, for incident angles of (a) 40° , (b) 50° and (c) 60° , respectively.

the refractive index n and extinction coefficient k of films at above the bandgap in order to compare the results.

The other two fits to the data of samples 2 and 3 are also performed assuming the four-phase (ambient/ $\text{Al}_x\text{Ga}_{1-x}\text{N}/\text{GaN}/\text{Sapphire}$) model. For GaN, refractive index function ($n+ik$) obtained by the fitting analysis for sample 1, which is also shown in Fig. 5.11, has been used. In Fig. 5.12 the complete coincidence between the measured and calculated data is shown for sample 2, and the parameters of the two samples, 2 and 3, are summarized in Table 5.4. The refractive indices n and extinction coefficient k as a function of photo-

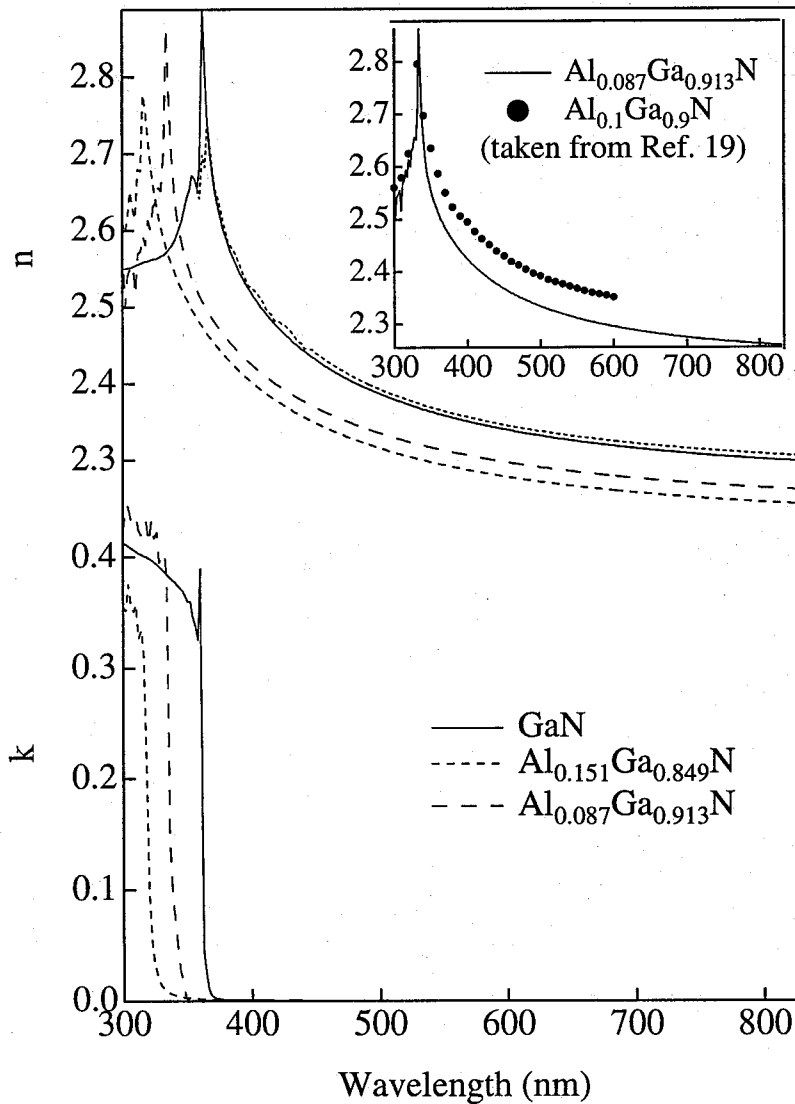


Figure 5.11: The optical constants of $Al_xGa_{1-x}N$ vs. wavelength. (a) the refractive indices determined by SE (b) the extinction coefficient k . The refractive indices of sample 2 and that from ref. 19 are shown in the inset.

energy are also calculated for both the samples, 2 and 3, and the data are plotted in Fig. 5.11(b) and (c) as dashed lines; in the inset of same figure refractive index function of sample 2 ($Al_{0.087}Ga_{0.913}N$) and that of $Al_{0.1}Ga_{0.9}N$ taken from ref. 19 are shown for comparison purpose. Our refractive index is found to be 2% smaller than that from ref. 19, this deviation perhaps arises from two distinct experimental method. We have further calculated SE data Δ using the refractive index ($n+ik$) and thicknesses of each layer and have shown in Fig. 5.13 by solid line. It is clear that the difference between the measured

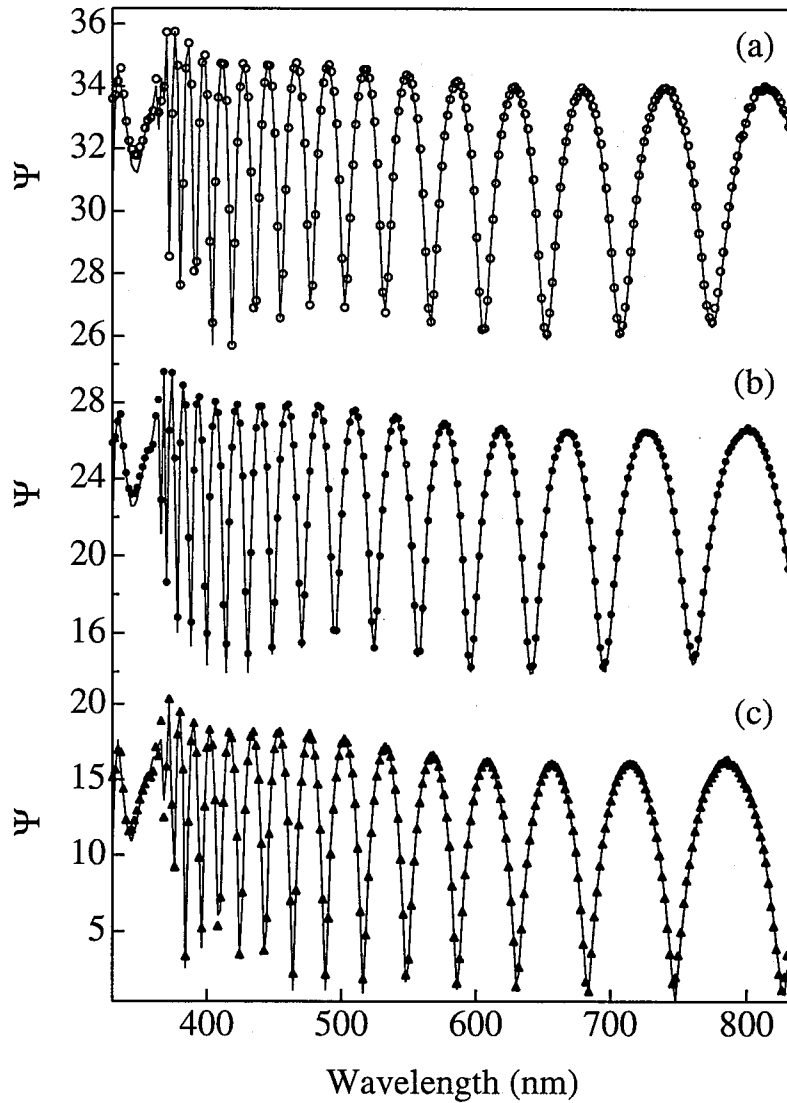


Figure 5.12: Measured (dotted line) and calculated (solid line) Ψ spectra of $Al_{0.087}Ga_{0.913}N/GaN$ on sapphire substrate, for incident angles of (a) 40° , (b) 50° and (c) 60° , respectively.

and calculated data is very small at the wavelength range measured. This indicates that our samples have good surface morphology and thin oxide film.

As shown in Table 5.4, the thicknesses obtained by SE and SEM are very close. Therefore, it is proved that our model adequately describes the measured data. The exciton energies have been obtained from Eq. 5.10, where the term $\frac{\hbar^2 k^2}{m^*} \omega_e$ has been neglected because of its extremely small value compared to term ω_e^2 and this energy value of sample 1 obtained is in agreement with our previous result for GaN. The exciton energy is also found to increase

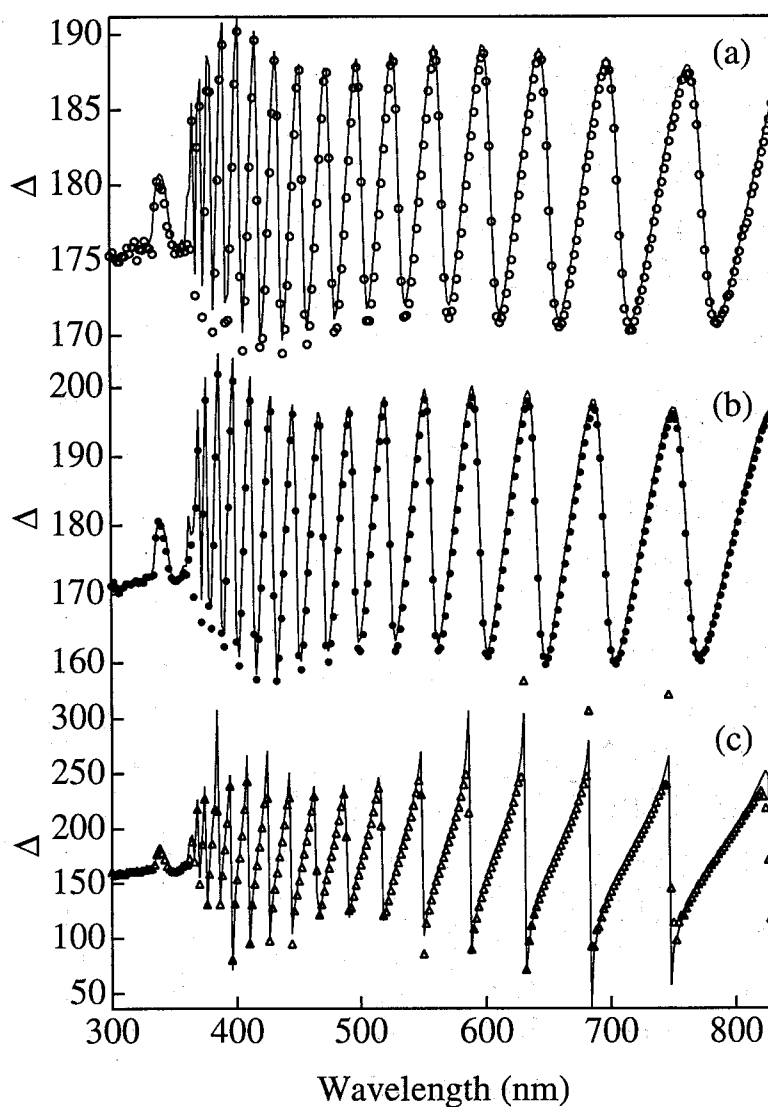


Figure 5.13: Measured (dotted line) and calculated (solid line) Δ spectra of sample 3 using the refractive index ($n+ik$) and thicknesses of films determined by fitting, for incident angle of (a) 40°, (b) 50° and (c) 60°, respectively.

with composition x .

5.4 Conclusion

Using an accurate film thickness which can be obtained by SE, one can determine optical functions of GaN by both SE and transmission method leading to the same results in the common wavelength region. The free exciton absorption in high-quality GaN sample is evidently observed at room temperature, with the transition energy at about 3.44 eV.

However, the deep level absorption near 2.0 eV is not observed.

The refractive indices n_{\perp} and n_{\parallel} as a function of wavelength over the wavelength range of 370 to 820 nm have obtained. The calculated spectra of the refractive indices n_{\perp} and n_{\parallel} are also analyzed using the first-order Sellmeier equation. The values of the high-frequency dielectric constant obtained are 5.14 for ($E \perp c$) and 5.31 for ($E \parallel c$). These values are close to the direct experimental observations (5.35).

Young's modulus of GaN film on sapphire substrate using the nano-indentation experiment have been estimated, and found that the maximum shear stress depends on the quality of the crystal. The maximum shear stress is 5.4 GPa for the high-quality GaN film. The "true-hardness" of GaN film is 53.6 GPa, which is larger than that of $In_{0.1}Ga_{0.9}N$ film on sapphire, and smaller than that of sapphire.

The optical constants of $Al_xGa_{1-x}N$ can be accurately expressed as the sum of Sellmeier dispersion equation and a free exciton below the fundamental band edge. The free exciton energy of $Al_xGa_{1-x}N$ has been obtained by simultaneously fitting to SE data Ψ measured at three angles of incidence, 40°, 50° and 60°. The values obtained vary from 3.44 to 3.95 eV when the composition x varies from 0 to 0.151.

References

- [1] S. Nakamura, T. Mukai, and M. Senoh, *Appl. Phys. Lett.* **64**, 1687 (1994).
- [2] S. Nakamura, M. Senoh and T. Mukai: *Jpn. J. Appl. Phys.* **32**, L8 (1993).
- [3] S. Nakamura, M. Senoh, S. Nagahama, N. Iwasa, T. Yamada, T. Matsushita, H. Kiyoku and Y. Sugimoto: *Jpn. J. Appl. Phys.* **35**, L217 (1996).
- [4] E. Ejder: *Phys. Status Solidi A***6**, 445 (1971).
- [5] S. Logothetidis, J. Petalas, M. Cardona and T. D. Moustakas: *Phys. Rev. B* **50**, 18 017 (1994).
- [6] S. Nakamura, M. Senoh, S. I. Nagahama, N. Iwasa, T. Yamada, T. Matsushita, H. Kiyoku, and Y. Sugimoto, *Jpn. J. Phys.* **35**, L74 (1996).
- [7] E. Ejder, *Phys. Status Solidi A***6**, 445 (1971).
- [8] L. Balagurov and P. J. Chong, *Appl. Phys. Lett.* **68**, 43 (1996).
- [9] G. E. Jellison, Jr., M. F. Chisholm and S. M. Gorbatkin, *Appl. Phys. Lett.* **62**, 3348 (1993).
- [10] S. Adachi, H. Kato, A. Moki and K. Ohtsuka, *J. Appl. Phys.* **75**, 478 (1994).
- [11] R. Nowak, T. Soga and M. Umeno, *Thin Solid Films* **295**, 193 (1997).
- [12] E. R. Weppelmann, J. S. Field and M. V. Swain, *J. Mater. Res.* **8**, 830 (1993).
- [13] *Handbook of Optical Constant of Solids II.* edited by E. D. Palik (Academic, New York, 1991).

CHAPTER 5. GaN and Al_xGa_{1-x}N on sapphire substrates

- [14] G. E. Jellison, Jr., Appl. Opt. **30**, 3354 (1991).
- [15] R. Swanepoel, J. Phys. E **16**, 1214 (1983).
- [16] M. Tchounkeu, O. Briot, B. Gil, J. P. Alexis and R. Aulombard, J. Appl. Phys. **80**, 5352 (1996).
- [17] P. Lautenschlager, M. Garriga, L. Vina, and M. Cardona, Phys. Rev. B **36**, 4821 (1987).
- [18] D. den Engelsen: J. Opt. Soc. Am. **61**, 1460 (1971).
- [19] H. Amano, N. Watanabe, N. Koide and I. Akasaki: Jpn. J. Appl. Phys. **32**, L1000 (1993).
- [20] S. Ninomiya and S. Adachi: Jpn. J. Appl. Phys. **33**, 2479 (1994).
- [21] D. T. F. Marple: J. Appl. Phys. **35**, 539 (1964).
- [22] L. Patrick and W. J. Choyke: Phys. Rev. B **2**, 2255 (1970).
- [23] S. Strite and H. Morkoc: J. Vac. Sci. & Technol. B **10**, 1237 (1992).
- [24] S. Fischer, C. Wetzel, E. E. Haller and B. K. Meyer: Appl. Phys. Lett. **67**, 1298 (1995).
- [25] E. R. Weppelmann, J. S. Field and M. V. Swain, J. Mater. Res. **8**, 830 (1993).
- [26] K. L. Johnson, Contact Mechanics (Cambridge University Press, Cambridge, 1985).
- [27] R. Thokala and J. Chaudhuri, Thin Solid Films **266**, 189 (1995).
- [28] Trevor F. Page, Warren C. Oliver and Carl J. McHarge, J. Mater. Res. **7**, 450 (1992).
- [29] M. Sakai, Acta Metall. Mater. **41**, 1759 (1993).
- [30] M. Erman, J. B. Theeten, N. Vodjdani, and Y. Demay, J. Vac. Sci. Technol. B, **1**, 328 (1983).

CHAPTER 5. GaN and $Al_xGa_{1-x}N$ on sapphire substrates

- [31] C. C. Kim, J. W. Garland, H. Abad, and P. M. Raccah, Phys. Rev. B **45**, 11 749 (1992).

Chapter 6

Inhomogeneous TiO₂ thin films

6.1 Introduction

Titanium dioxide is a large band gap semiconductor of exceptional stability and has diverse industrial applications. In recent years, sol-gel derived nanocrystalline TiO₂ thin films of anatase phase are becoming of increasing importance because of their ease of preparation and potential application in the areas of photovoltaics, sensing devices, photocatalysis and microelectronics.¹⁾ Consequently, the determination of the optical constants and evaluation of microstructural features such as surface roughness in these films are important.

Wide variations in the optical and physical properties of TiO₂ thin films deposited by different techniques have been reported.²⁾ The aim of this work is to study the optical constants and depth profile of sol-gel derived TiO₂ thin films in order to better understand their optical properties. Spectroscopic ellipsometry (SE), which is known to be a very useful and non-destructive technique to investigate the optical properties of inhomogeneous films, has been used together with transmission spectroscopy to study our films. Ellipsometric determination of optical constants of inhomogeneous TiO₂ films deposited by different evaporation techniques has been reported by various authors where they assumed a linear variation in the refractive index along the thickness of the film.^{3,4)} In this work, a four-phase model (air/rough surface layer/inhomogeneous TiO₂ layer/substrate) has been used to fit the SE data, taken in the wavelength range of 260 - 830 nm. In the inhomogeneous layer, void distribution has been assumed to vary instead of the variation in the refractive index (n) and the unknown dielectric function of TiO₂ is described by a

single oscillator form. An excellent agreement between the calculated and measured data of SE in the 335 - 830 nm wavelength range has been obtained. However, determination of the extinction coefficient k by fitting SE data, with the dielectric function being described by a single oscillator, is not very accurate near and above the fundamental band gap. For the accurate determination of k , Forouhi and Bloomer derived a formalism of $k(\lambda)$ above the fundamental band gap based on quantum-mechanical theory of absorption.⁵⁾ Kim used this formalism with spectroscopic ellipsometry and transmission spectroscopy for the simultaneous determination of n , k and void distribution of electron-beam (EB) evaporated amorphous TiO_2 thin film.⁶⁾ In this work we calculated the extinction coefficient for both the amorphous and nanocrystalline TiO_2 thin films from transmission spectrum using the refractive index, thickness and void of each layer determined by SE. Our as-deposited and low temperature annealed (400°C) films were amorphous as observed by X-ray diffraction (XRD) analysis. At higher annealing temperature (600°C), films were found to be polycrystalline with crystal structure matching with the anatase modification of TiO_2 lattice. Scanning electron micrograph (SEM) showed the 600°C temperature annealed sample to be nanocrystalline with porous structure. Details of the experimental and theoretical procedures are described in the subsequent sections and the results obtained are compared with those reported by others for TiO_2 films deposited by different techniques.

6.2 Experimental

TiO_2 thin films were deposited on vitreous silica substrate by sol-gel method using titanium tetra-isopropoxide, $\text{Ti}(\text{C}_3\text{H}_7\text{O})_4$, as the starting material for Ti. The details of the sol solution preparation are described elsewhere.⁷⁾

Films were coated on vitreous silica substrate by dip-coating method with a pulling speed of 0.1 mm/sec. The films coated were dried at 80°C for 15 minutes and heat treated at 400°C for 1 h and the process was repeated for 5 times. Two films thus obtained were annealed for 6 hours at 400 and 600°C , and hereafter will be referred to as sample 1 and sample 2, respectively.

The measurements of spectroscopic ellipsometry were carried out at an angle of incidence of 75° in the wavelength range of 260 - 830 nm. The automatic ellipsometry used was of rotating analyzer type, fitted with a 75 W xenon lamp as a light source. Back surface of the substrates were roughened and blackened before ellipsometric measurements to eliminate back surface light reflection. Transmission spectrum of the samples was taken before SE measurements over the wavelength range of 300 - 1600 nm for the accurate determination of extinction coefficient k . The transmission spectrum of the bare vitreous silica substrate was also taken to determine its refractive index. All the measurements were performed at room temperature.

6.3 Theoretical treatment

The ellipsometric parameters Ψ and Δ are defined as usual from the ratio of reflected amplitudes for s and p polarization

$$\rho = \frac{r_p}{r_s} = \frac{|r_p|}{|r_s|} e^{i(\delta_p - \delta_s)} = \tan \Psi e^{i\Delta} \quad (6.1)$$

In the case of an inhomogeneous film of thickness d upon a nonabsorbing substrate with index of refraction n_3 , in a medium with refractive index n_0 , refractive index of the film is not uniform but varies as a function of distance along the thickness of the film. The refractive index profile for such a system is illustrated in Fig. 6.1. Under the simplifying assumption that the reflection of light from the interior of the film can be ignored, the detailed expressions of Ψ and Δ have been given by Z.⁸⁾ It has also been shown by Carniglia that ellipsometric data at half-wave (HW) points, defined as wavelengths that are multiples of twice the optical thickness, in the $\tan \Psi$ spectrum (hereafter referred to as $\tan \Psi(HW)$), offers a sensitive measure of the degree of inhomogeneity. Under the condition of extinction coefficient $k=0$, $\cos \Delta=1$ and the $\tan \Psi$ (HW) results in expression⁸⁾

$$\tan \Psi (HW) = \frac{(n_{p0}n_{p2} - n_{p1}n_{p3})}{(n_{p0}n_{p2} + n_{p1}n_{p3})} \bigg/ \frac{(n_{s0}n_{s2} - n_{s1}n_{s3})}{(n_{s0}n_{s2} + n_{s1}n_{s3})} \quad (6.2)$$

where

$$n_{si} = \left(n_i^2 - n_0^2 \sin^2 \theta_0 \right)^{1/2},$$

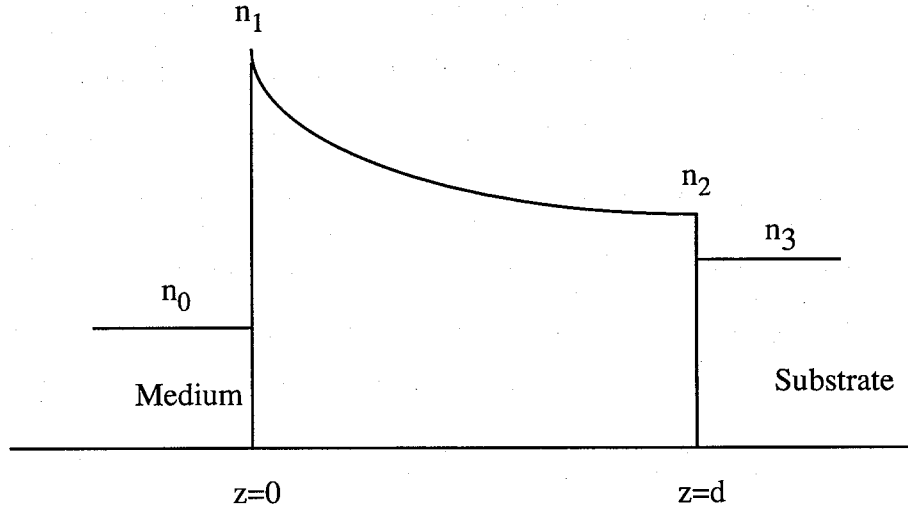


Figure 6.1: Typical refractive index profile of an inhomogeneous film of thickness d upon a non-absorbing substrate with refractive index n_3 in a medium with refractive index n_0 . Refractive index of the film varies from n_1 at the outer surface of the film to n_2 at the inner surface.

$$n_{pi} = n_i^2 / (n_i^2 - n_0^2 \sin^2 \theta_0)^{1/2}.$$

Here θ_0 is the angle of incidence, n_1 and n_2 are the refractive indices at the outer and inner surfaces of the inhomogeneous layer, respectively. In particular, when the film is homogeneous, i.e. $n_1 = n_2$, $\tan \Psi$ (HW) is given by

$$\tan \Psi (HW) = \frac{(n_{p0} - n_{p3})}{(n_{p0} + n_{p3})} \bigg/ \frac{(n_{s0} - n_{s3})}{(n_{s0} + n_{s3})} = \tan \Psi_s, \quad (6.3)$$

showing that for homogeneous film $\Psi(HW)$ is equal to Ψ_s , the amplitude reflectance ratio of the uncoated substrate, and is independent of the index of the film. Thus, from the difference between Ψ_s and $\Psi(HW)$, one can get an idea about the degree of inhomogeneity of a film which is defined by $\Delta n / \bar{n}$; here \bar{n} is the average refractive index of the film and $\Delta n = n_1 - n_2$.

To demonstrate the effect of degree of inhomogeneity on $\tan \Psi$ spectrum, a series of $\tan \Psi$ spectrum is drawn in Fig. 6.2 for single-layer films (solid lines), together with the $\tan \Psi_s$ spectrum (dashed line), with $\Delta n / \bar{n}$; here \bar{n} varying from -15% to +15% in steps of 7.5%, for an incidence angle of 75° . Here, the average refractive index of the film is assumed to be 2.3, and that of the substrate to be 1.5. It is clearly seen from Fig. 6.2 that the spectrum of $\tan \Psi$ at the HW points shift from values above that of the $\tan \Psi_s$ spectrum to values below

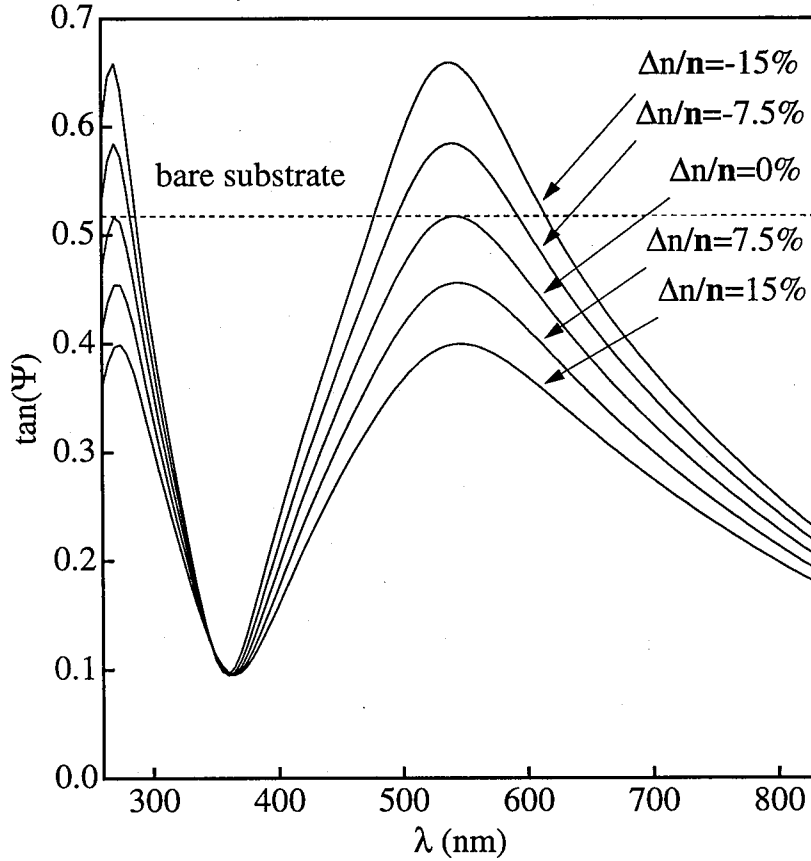


Figure 6.2: Calculated $\tan\Psi$ spectrum (solid curves) for films together with the $\tan\Psi_s$ spectrum (dashed line) for the substrate with $\Delta n/\bar{n}$ (\bar{n} , the average refractive index) varying from -15% to $+15\%$ in steps of 7.5% for an angle of incidence of 75° . The average refractive index \bar{n} of the film is assumed to be 2.3 and that of the substrate to be 1.5 .

that of $\tan\Psi_s$, as $\Delta n/\bar{n}$ varies from -15% to $+15\%$. Two conclusions can be drawn from this figure: i) the larger the degree of inhomogeneity $\Delta n/\bar{n}$, the larger is the difference between $\tan\Psi_s$ and $\tan\Psi(\text{HW})$, ii) position of $\tan\Psi(\text{HW})$ points relative to $\tan\Psi_s$ spectrum depends upon the sign of $\Delta n/\bar{n}$, i.e., for $n_1 > n_2$, $\tan\Psi(\text{HW}) < \tan\Psi_s$ and vice versa. Another point worth noting is that there is no significant effect of the value of average refractive index on the value of $\tan\Psi(\text{HW})$ which has a strong dependence on the degree of inhomogeneity. This point is clearly depicted in Fig. 6.3 where the $\tan\Psi$ spectra for single-layer films (solid lines), together with the $\tan\Psi_s$ spectrum (dashed line), are drawn with average refractive index varying from 1.7 to 2.5 , and keeping the degree of inhomogeneity $\Delta n/\bar{n}$ constant (-15%). With the increase in the average refractive index, small increase in the value of $\tan\Psi(\text{HW})$ is observed. However, compared to the large change in $\tan\Psi(\text{HW})$ ($\sim 40\%$) for

CHAPTER 6. Inhomogeneous TiO_2 thin films

a relatively small change in $\Delta n/\bar{n}$ (15%), this change in $\tan\Psi(\text{HW})$ ($\sim 5\%$) for a relatively large change (47%) in \bar{n} is quite small. Furthermore, all $\tan\Psi(\text{HW})$ points remain on the same side of the $\tan\Psi_s$ spectrum despite a large change in \bar{n} and thus the sign of $\Delta n/\bar{n}$ remains unaffected by the change in \bar{n} . It should be mentioned here that the above analysis is valid only for situations where the substrate has a lower refractive index than that of the film, i.e., $n_3 < \bar{n}$, and the incidence angle is 75° . This particular case is discussed because it matches with our problem where we have used vitreous silica substrate which has an average refractive index (1.5) lower than that for TiO_2 (2.2 - 2.6).²⁾ For TiO_2 films on substrates with higher refractive indices, such as Si, the relative positions of $\tan\Psi$ and $\tan\Psi_s$ spectra will change and the above discussion has to be modified. A change in the incidence angle will also affect the relative positions of $\tan\Psi$ and $\tan\Psi_s$ spectra.

Using the same assumption invoked earlier in the calculations of $\tan\Psi$ in SE, i.e., the reflection of light from the interior of the film can be ignored, the amplitude transmission at normal incidence can be written as

$$t = \frac{t_{10}t_{23} \exp(-i\delta)}{1 + r_{10}r_{23} \exp(-i2\delta)}, \quad (6.4)$$

where t_{10} and t_{23} are the Fresnel transmission coefficients at the medium-film and the film-substrate interfaces, respectively, and r_{10} and r_{23} are the corresponding Fresnel reflection coefficients, and are given by

$$t_{10} = \frac{2n_0}{n_0 + n_1}, \quad t_{23} = \frac{2n_2}{n_2 + n_3},$$

and

$$r_{10} = \frac{n_0 - n_1}{n_0 + n_1}, \quad r_{23} = \frac{n_2 - n_3}{n_2 + n_3}.$$

The phase angle δ is given by

$$\delta = \frac{2\pi}{\lambda} \int_0^d n(z) dz.$$

The transmission T can be written as

$$T = \frac{n_1 n_2}{n_0 n_2} t t^*. \quad (6.5)$$

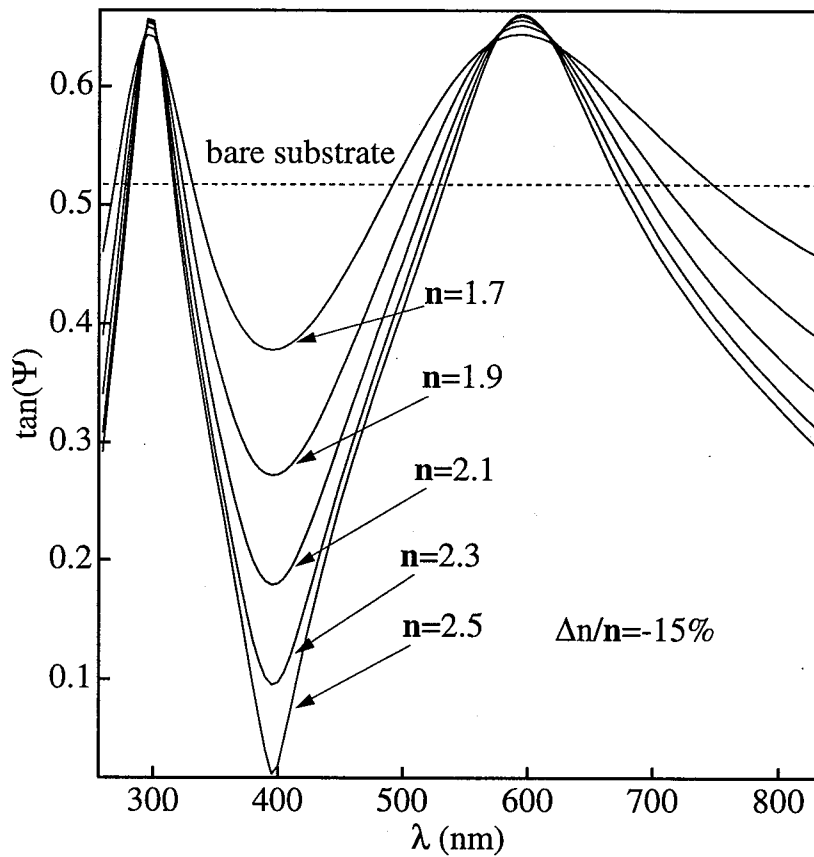


Figure 6.3: Calculated $\tan\Psi$ spectrum (solid lines) for films, together with $\tan\Psi_s$ spectrum (dashed line) for the substrate, with average refractive index varying from 1.7 to 2.5. The degree of inhomogeneity $\Delta n/n$ (n , the average refractive index \bar{n}) for all the films is considered to be constant (-15%).

The Bruggeman effective-medium theory (EMT), considered as an important tool to investigate inhomogeneous film, is used to calculate the effective dielectric function of the film. The mathematical formula can be expressed as:⁹⁾

$$(1 - f_v) \frac{\epsilon_m - \epsilon}{\epsilon_m + 2\epsilon} + f_v \frac{1 - \epsilon}{1 + 2\epsilon} = 0, \quad (6.6)$$

where ϵ_m is the dielectric function of main constituent material and f_v is the volume fraction of void. In this equation the dielectric function of void is taken to be 1. In our SE data analysis, the unknown dielectric function of TiO₂ is described by a single oscillator

$$\epsilon = \epsilon'_\infty + \frac{(\epsilon_s - \epsilon'_\infty) \omega_t^2}{\omega_t^2 - \omega^2 - i\Gamma_0 \omega} \quad (6.7)$$

where ϵ'_∞ represents the high-frequency dielectric constant, ϵ_s is the oscillator strength, ω_t the frequency and Γ_0 the damping factor of the oscillator. The unknown parameters

can be numerically determined by minimizing the following mean squares deviation with a regression program (unbiased):

$$\delta^2 = \frac{1}{2N - P} \sum_{i=1}^N \left[\left(\tan \Psi_i^{\text{exp}} - \tan \Psi_i^{\text{cal}} \right)^2 + \left(\cos \Delta_i^{\text{exp}} - \cos \Delta_i^{\text{cal}} \right)^2 \right], \quad (6.8)$$

where N is the number of data points and P is the number of unknown model parameters.

6.4 Results and discussion

6.4.1 Spectroscopic ellipsometry

A four-phase structure (air/rough surface layer/inhomogeneous TiO₂/substrate) as shown in Fig. 6.4 has been used in the simultaneous fitting of measured parameters Δ and Ψ of SE. The roughness layer on the surface was modeled as an effective mixture of 50% TiO₂ and 50% void. Inhomogeneity of a film results from the non-uniform packing density of the film which is usually expressed by the volume fraction of void f_v . In our fitting analysis f_v is varied from $f_{v0}=0$ at the outer surface of the film to f_{vi} at the inner surface. This simplifies the calculation than considering the refractive index varying along the thickness of the film since f_v is a function of distance only while refractive index is a function of both distance and wavelength. However, it should be noted that our assumption of f_v varying from zero at the outer surface to f_{vi} at the inner surface is only for the sake of obtaining the distribution of dielectric function along the depth of the film by fitting to ellipsometric data and shows only relative variation in the void fraction along the thickness of the film. The change in refractive index along the depth of the film will follow the change in f_v . After obtaining the refractive index by fitting to SE data, actual void distribution along the depth of the film has been calculated using the "void-free" refractive index of anatase TiO₂ as Kim did.⁶⁾

Measured (solid circles and plus sign) and fitted (solid lines) $\cos\Delta$ (top) and $\tan\Psi$ (bottom) spectra of samples 1 and 2; together with the calculated data of bare substrate (dashed lines), are shown in Fig. 6.5. An excellent agreement between the experimental and fitted $\cos\Delta$ and $\tan\Psi$ spectra for both the samples have been obtained. From this figure, HW fringes at 350 and 550 nm for sample 1 and at 345 and 500 nm for sample 2 are observed.

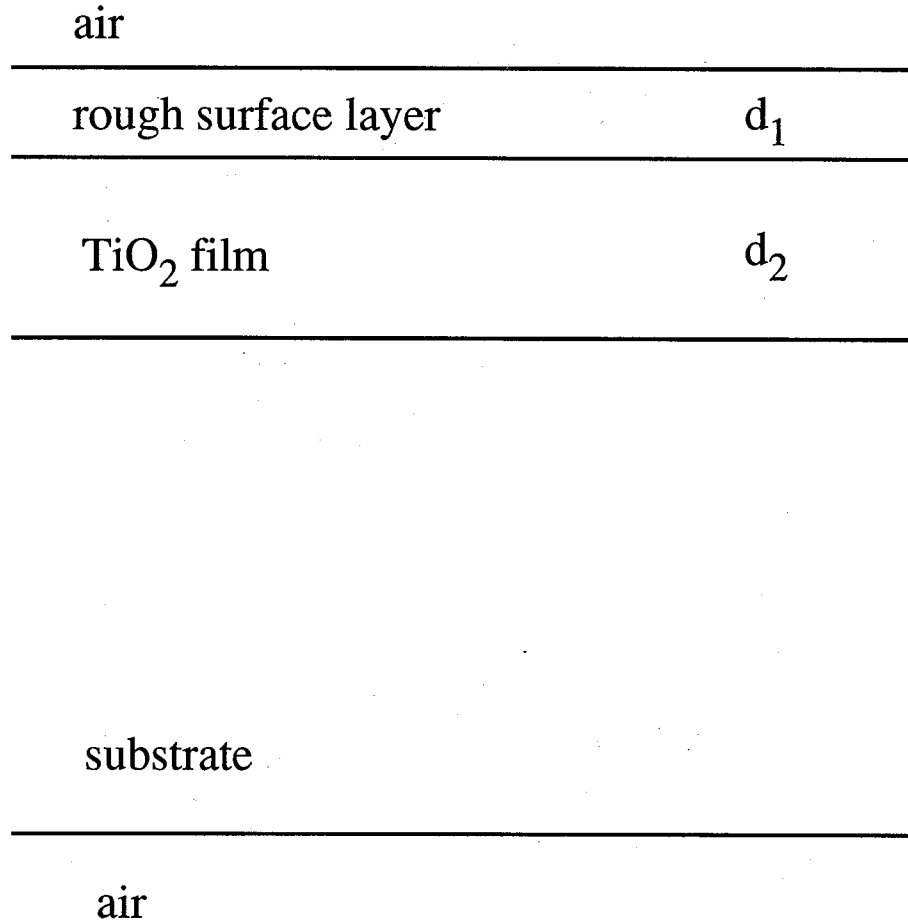


Figure 6.4: Schematic diagram of the film structure used in SE fitting.

At wavelengths 550 and 500 nm, i.e., at the HW fringes for sample 1 and 2, respectively, $\cos\Delta \approx 1$ and $\tan\Psi(\text{HW}) \neq \tan\Psi_s$. $\cos\Delta \approx 1$ illustrates that extinction coefficient k of the films is close to zero in this region whereas $\tan\Psi(\text{HW}) \neq \tan\Psi_s$ shows the inhomogeneity of the films. For both the films $\tan\Psi(\text{HW}) < \tan\Psi_s$, indicating $n_1 > n_2$ for both the films according to our analysis discussed in the previous section, and larger difference between $\tan\Psi(\text{HW})$ and $\tan\Psi_s$ indicates larger inhomogeneity for sample 2, which has a nanocrystalline structure of anatase phase, than for sample 1 which is amorphous, as observed by X-ray diffraction analysis.

Table 6.1 shows the best fit model parameters used in the simulation of $\cos\Delta$ and $\tan\Psi$ spectra. The high frequency dielectric constants obtained are 2.83 and 3.7 for samples 1 and 2, respectively. However, as pointed out by Gerfin et al. for ITO films,¹⁰⁾ here also ϵ'_∞ does not represent the true high-frequency dielectric constant ϵ'_∞ . The optimized dispersion

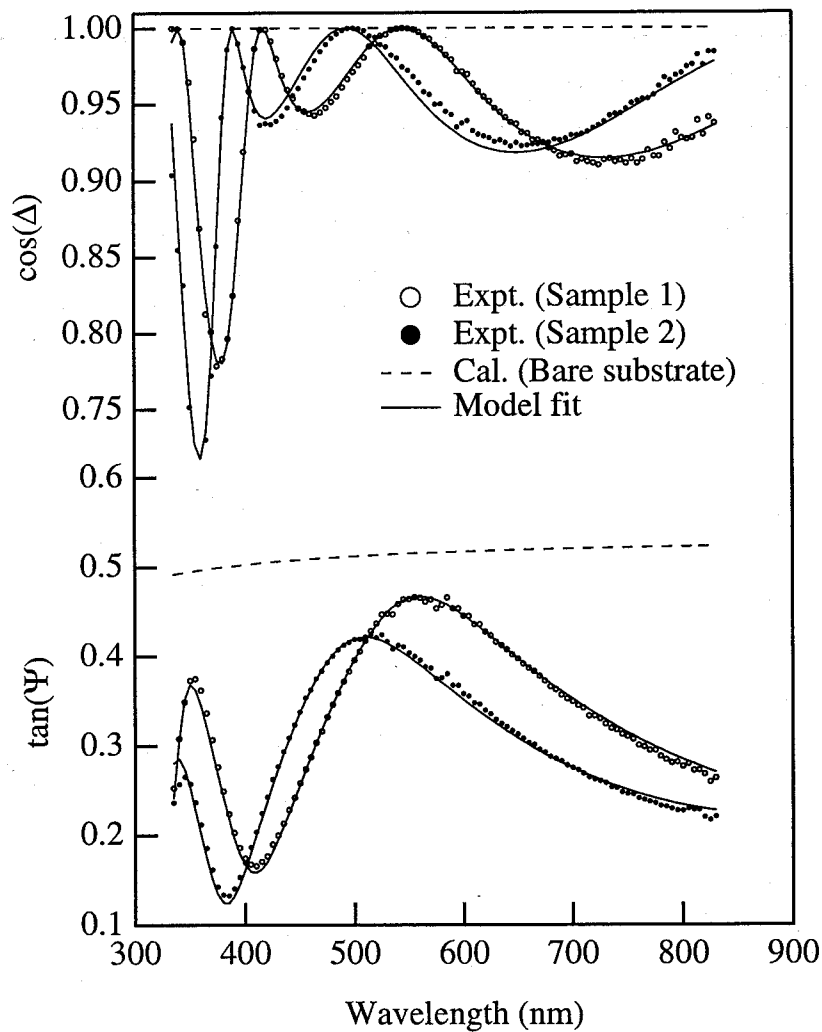


Figure 6.5: Measured (solid circles and plus sign) and fitted (solid lines) $\cos\Delta$ (top) and $\tan\Psi$ (bottom) spectra of samples 1 and 2, together with the calculated data of bare substrate (dashed lines).

formula can be regarded only as a mathematical description of the optical properties below the band edge region of the semiconductor. The value of ϵ'_∞ can be determined graphically, as shown in Fig. 6.6 and are found to be 4.16 and 4.39 for samples 1 and 2, respectively, which are close to that determined by S. Y. Kim for “void-free” value (4.8) of electron-beam-evaporated TiO_2 thin film. The thickness of sample 2 is smaller than that of sample 1 (from Table 6.1), indicating higher packing density and larger refractive index for sample 2 than for sample 1, may be due to the crystalline nature of sample 2, and is consistent with the results reported by Vorotilov et al. for sol-gel derived TiO_2 thin films.¹¹⁾ In

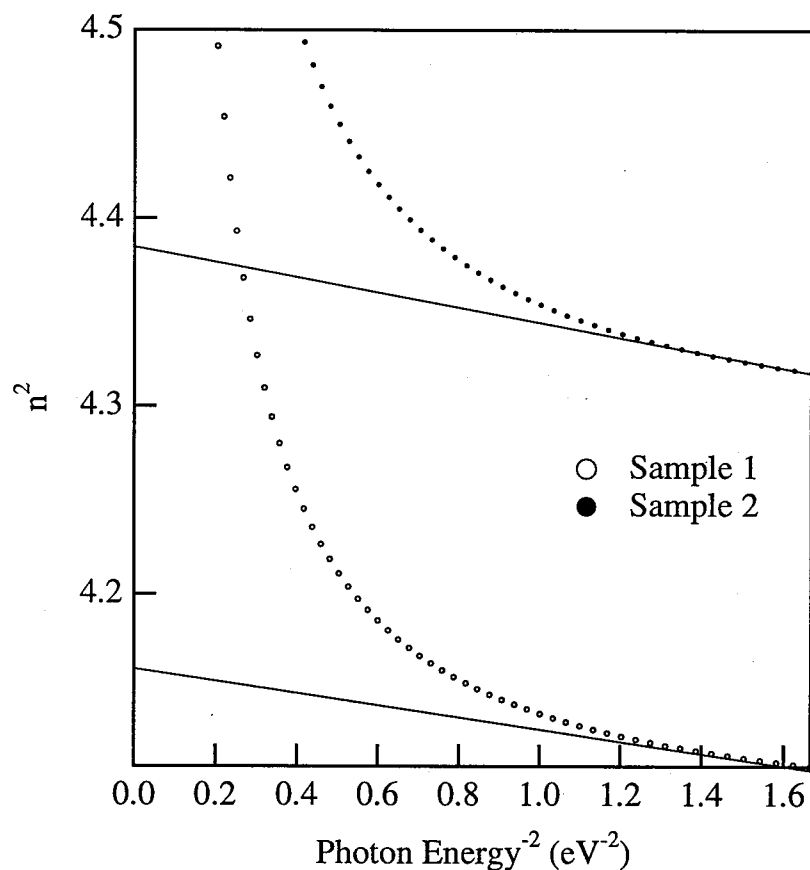


Figure 6.6: Graphical determination of the high-frequency dielectric constant of the two samples.

Table 6.1: Best-fit model parameters of the sol-gel derived TiO_2 thin films on vitreous silica substrate determined by spectroscopic ellipsometry. The f_{vi} is the volume fraction of void at the inner surface of layer 2. The 90% confidence limits are given with (\pm).

Sample	ϵ'_{∞}	ϵ_s	ω_t (eV)	Γ_0 (eV)	f_{vi}	d_1 (nm)	d_2 (nm)	δ
1	28.3 ± 0.03	4.07 ± 0.05	4.39 ± 0.03	0.20 ± 0.01	0.097 ± 0.002	4.74 ± 0.03	148.74 ± 0.001	0.005
2	3.70 ± 0.06	4.52 ± 0.1	4.06 ± 0.07	0.25 ± 0.02	0.210 ± 0.003	2.19 ± 0.03	133.41 ± 0.001	0.008

Fig. 6.7 we show the grading profiles of refractive indices obtained for samples 1 and 2 at 500 nm wavelength. Almost linear index gradient along the depth of the films has been obtained. Note the larger index gradient and smaller refractive index at the inner surface of sample 2, indicate severer inhomogeneity of nanocrystalline film, as has also been found

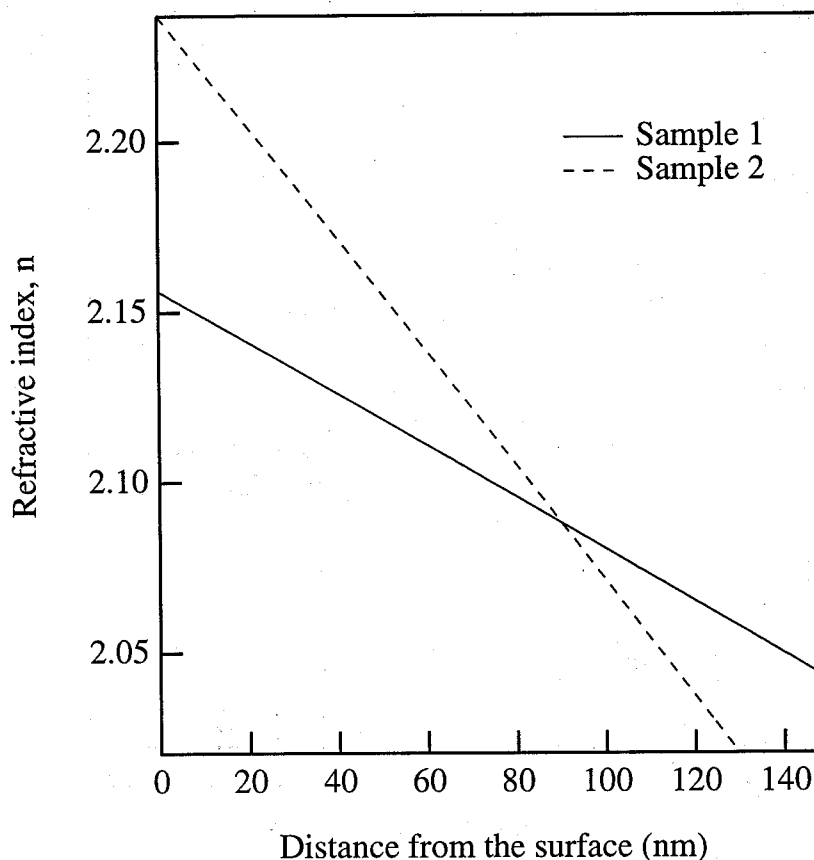


Figure 6.7: Depth profile of the refractive indices at 500 nm wavelength for the two samples.

by Susan et al. for sol-gel derived $\text{Pb}(\text{Zr},\text{Ti})\text{O}_3$ film.¹²⁾ The higher refractive index at the outer surface of the films can be explained in terms of densification and crystallization of the as deposited films which begin at the surface and gradually progress towards the depth of the film during the course of annealing.¹³⁾ Actual void distribution along the thickness of the film has been calculated using the refractive index of anatase TiO_2 ⁶⁾ and is found to vary from 28% to 35% from the outer surface to the inner surface of the film for sample 1 and from 25% to 38% for sample 2 for the same. These values are much larger than that reported for EB evaporated TiO_2 thin film (16%).⁶⁾ The presence of high percentage of void is a common feature for sol-gel derived oxide thin films. Figure 6.8 shows the variation of the degree of inhomogeneity $\Delta n/\bar{n}$ with photon energy for both the samples, obtained by our fitting results. It shows much larger degree of inhomogeneity $\Delta n/\bar{n}$ for sample 2 than for sample 1 and is consistent with Fig. 2 where larger difference between $\tan\Psi(\text{HW})$ and

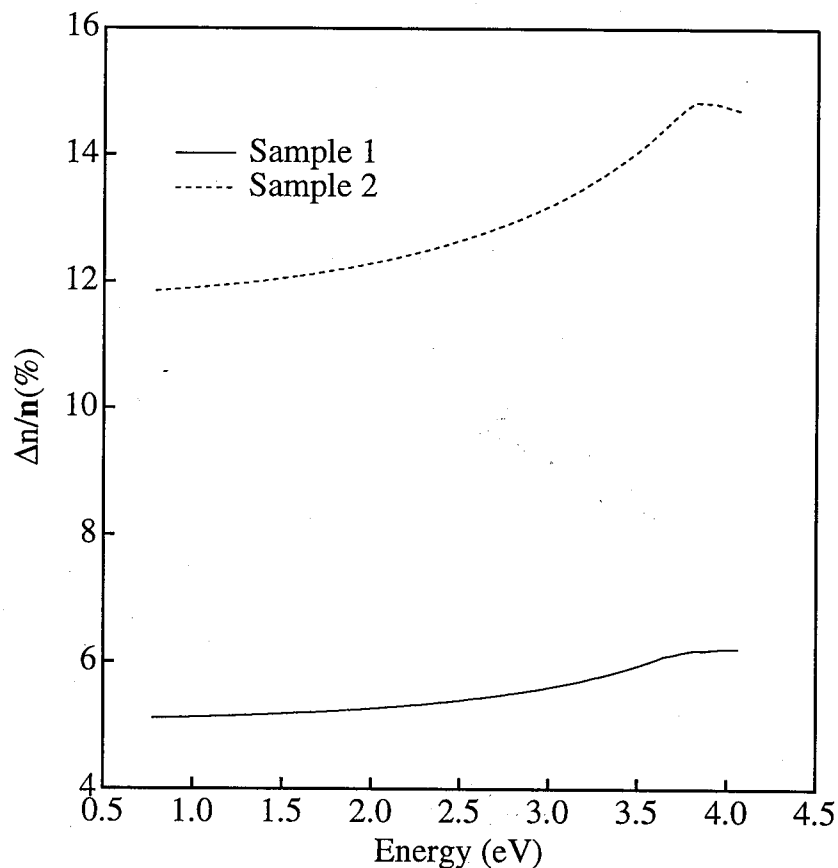


Figure 6.8: Variation of the degree of inhomogeneity $\Delta n/n$ (n , the average refractive index \bar{n}) with photon energy for both the samples.

$\tan\Psi_s$ has been observed for sample 2 than for sample 1, indicating larger inhomogeneity for sample 2. Furthermore, the degree of inhomogeneity of sample 2 varying from 12% to 14% is much larger than those reported for TiO_2 films deposited by EB evaporation (3 - 5 %) and rf sputtering (5 %) techniques²⁾ while that for sample 1 varying from 5% to 6% is close to those reported values. This shows that high temperature annealing severely degrades the homogeneity of the film. One reason for the higher degree of inhomogeneity for sol-gel derived thin films may be that in this method films are coated layer by layer with each coating followed by drying of the films at sufficiently high temperature ($>100^\circ\text{C}$) while in other techniques, such as, EB evaporation and rf sputtering, films are deposited in a single run. However, the underlying mechanism that further deteriorates the homogeneity of the film upon annealing at high temperatures is yet to be investigated.

6.4.2 Transmission spectroscopy

For the multilayer structure of our film, we use potential transmission Ψ according to Berning et al. which is given by¹⁴⁾

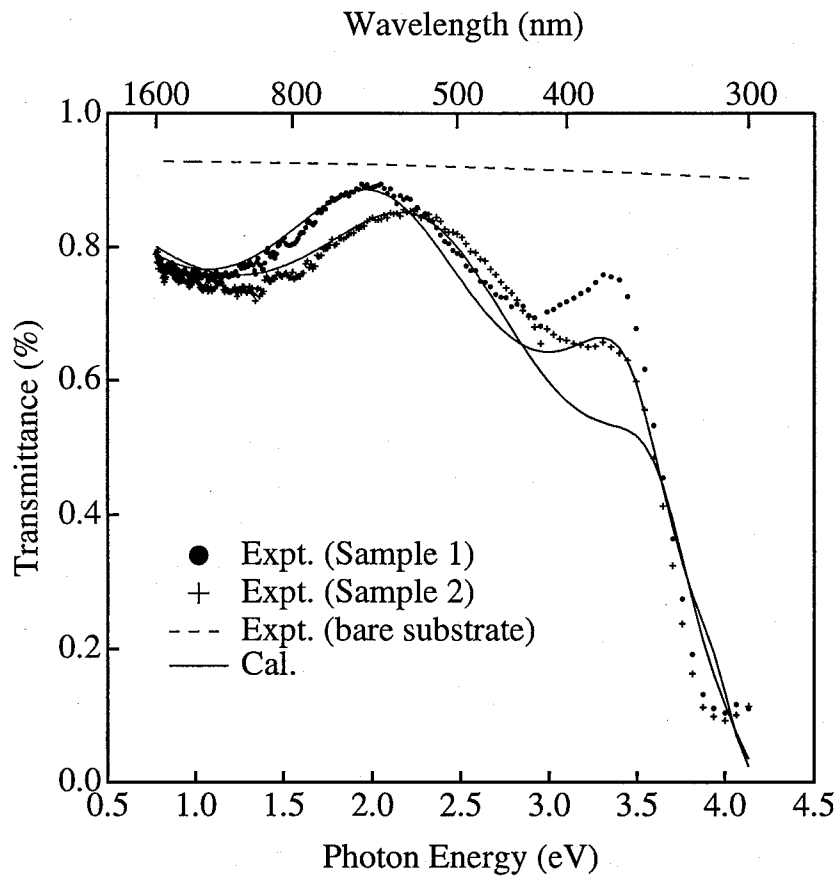


Figure 6.9: Measured (solid circles and plus sign) and calculated (solid lines) transmission spectra of both the samples in the wavelength range of 300 - 1600 nm. The solid lines are obtained by using the extrapolated optical constants and thicknesses determined by SE. The dashed line shows the measured transmission spectrum of the bare substrate.

$$\Psi = \frac{T}{1 - R} = \prod_i \frac{T_i}{1 - R_i}, \quad (6.9)$$

where T_i , R_i are the transmission and reflection of i th layer, respectively. Figure 6.9 shows the measured (solid circles and plus sign) and calculated (solid lines) transmission spectra of both the samples together with the measured transmission spectrum of the bare substrate (dashed line) in the wavelength range of 300 - 1600 nm. The solid lines are obtained by using the extrapolated optical constants, thicknesses and void distribution determined

by SE. Good agreement between the experimental and calculated data in the long wavelength region has been obtained while at the short wavelength region, the deviations of the calculation from the experimental data is due to the inaccurate extinction coefficient obtained by fitting SE data using a single oscillator which does not accurately reflect the effect of interband transitions occurring at and above 3.2 eV. It can be noted that the indirect band gap of anatase phase TiO_2 is about 3.2 eV.

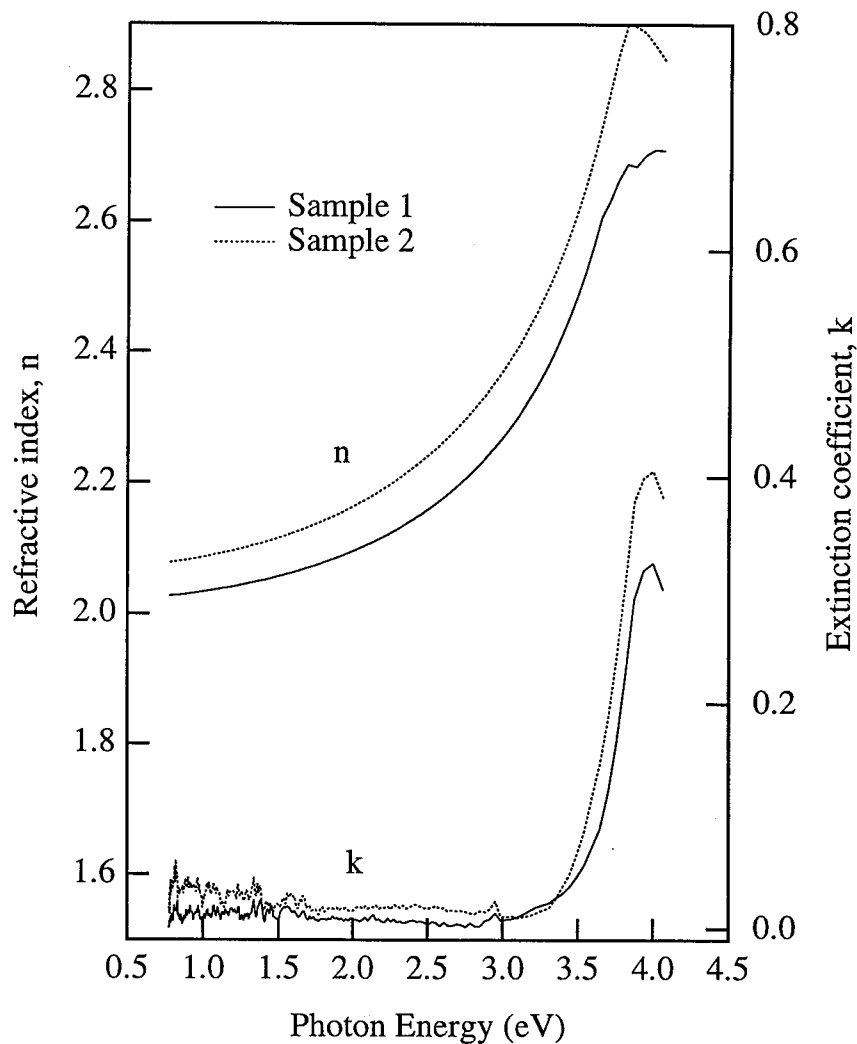


Figure 6.10: Refractive index n (top) and extinction coefficient k (bottom) spectra of the sample 1 (dashed lines) and 2 (solid lines).

The extinction coefficient $k(\lambda)$ for both the samples are obtained over the wavelength range 300 - 1600 nm from the transmission spectra, using the extrapolated refractive indices and structure parameters of the films obtained by SE. In Fig. 6.10 we show the refractive

index n (top) and extinction coefficient k (bottom) spectra for both the samples over the energy range 0.77 - 4.0 eV. Sample 2 shows larger refractive index than sample 1 and is attributed to the increase in packing density and crystallinity of the film at elevated temperature, which are evident from the thickness measurement and XRD analysis. This result is in good agreement with that by Suhail et al., for magnetron sputtered TiO₂ thin films deposited on vitreous silica substrate, where they reported similar increase in the refractive index with increasing annealing temperature.¹⁵⁾ Sharper increase in k above the fundamental band gap for sample 2 shows the crystalline nature of the film. Note the nonzero extinction coefficient of sample 2 at a much lower photon energy than the band gap energy indicates scattering effect in the nanocrystalline TiO₂ thin film.

6.5 Conclusions

Sol-gel derived TiO₂ thin films, both amorphous and nanocrystalline, are investigated for optical properties by spectroscopic ellipsometry and transmission spectroscopy. A method to fit simultaneously the measured parameters of SE, Ψ and Δ , for inhomogeneous thin film has also been described. Instead of the refractive index, volume fraction of void has been assumed to vary along the thickness of the film in the fitting analysis and an excellent fit has been obtained for both the amorphous and nanocrystalline TiO₂ films. Nearly linear refractive index gradient has been obtained for both the samples with sample 2 having a larger index gradient than sample 1 showing deterioration of homogeneity with increase in annealing temperature. The degree of inhomogeneity obtained are 5-6% and 12-14% for samples 1 and 2, respectively, and are higher than those reported for TiO₂ films deposited by EB evaporation (3 - 5 %) and rf sputtering (5 %) techniques. Extinction coefficients $k(\lambda)$ of the samples are calculated from the transmission spectra. Nonzero k values for sample 2 at photon energies much lower than the fundamental band gap energy (3.2 eV) show scattering effect in the nanocrystalline TiO₂ film.

References

- [1] M. Gratzel, "Nanocrystalline electronic junctions," in *Semiconductor Nanoclusters - Physical, Chemical and Catalytic Aspects*, P. V. Kamat, and D. Meisel, ed. (Elsevier, Netherlands 1997), pp. 353-461.
- [2] J. M. Bennett, E. Pelletier, G. Albrand, J. P. Borgogno, B. Lazarides, C. K. Carniglia, R. A. Schmell, T. H. Allen, T. Tuttle-Hart, K. H. Guenther, and A. Saxer, "Comparison of the properties of titanium dioxide films prepared by various techniques," *Appl. Opt.* **28**, 3303-3316 (1989).
- [3] G. Parjadis de Lariviere, J. M. Frigerio, J. Rivory, and F. Abeles, "Estimate of the degree of inhomogeneity of the refractive index of dielectric films from spectroscopic ellipsometry," *Appl. Opt.* **31**, 6059-6061 (1992).
- [4] J. P. Borgogno, F. Flory, P. Roche, B. Schmitt, G. Albrand, E. Pelletier, and H. A. Macleod, "Refractive index and inhomogeneity of thin films," *Appl. Opt.* **23**, 3567-3570 (1984).
- [5] A. R. Forouhi and I. Bloomer, "Calculation of Optical Constants, n and k , in the Interband region," in *Handbook of Optical Constants of Solids II*, E. D. Palik, ed. (Academic, Toronto 1991), chap. 7.
- [6] S. Y. Kim, "Simultaneous determination of refractive index, extinction coefficient and void distribution of titanium dioxide thin film by optical methods," *Appl. Opt.* **35**, 6703-6707 (1996).
- [7] M. M. Rahman, T. Miki, K. M. Krishna, T. Soga, K. Igarashi, S. Tanemura, and M. Umeno, "Structural and optical characterization of $Pb_xTi_{1-x}O_2$ film prepared by

CHAPTER 6. Inhomogeneous TiO_2 thin films

- sol-gel method," *Mater. Sci. Engg. B* **41**, 67-71 (1996).
- [8] C. K. Carniglia, "Ellipsometric calculations for nonabsorbing thin films with linear refractive-index gradients," *J. Opt. Soc. Am. A* **7**, 848-856 (1990).
- [9] D. E. Aspnes and J. B. Theeten, "Investigation of effective-medium models of microscopic surface roughness by spectroscopic ellipsometry," *Phy. Rev. B* **20**, 3292-3302 (1979).
- [10] T. Gerfin, and M. Gratzel, "Optical properties of tin-doped indium oxide determined by spectroscopic ellipsometry," *J. Appl. Phys.* **79**, 1722-1729 (1996).
- [11] K. A. Vorotilov, E. V. Orlova, and V. I. Petrovsky, "Sol-gel TiO_2 films on silicon substrates," *Thin Solid Films* **207**, 180-184 (1992).
- [12] T. M. Susan, J. Chen, K. Vedam, and R. E. Newnham, "In situ annealing studies of sol-gel ferroelectric thin films by spectroscopic ellipsometry," *J. Am. Ceram. Soc.* **78**, 1907-1913 (1995).
- [13] Y. Mishima, M. Takei, T. Uematsu, N. Matsumoto, T. Kakehi, U. Wakino, and M. Okabe, "Polycrystalline silicon formed by ultrahigh-vacuum sputtering system," *J. Appl. Phys.* **78**, 217-223 (1995).
- [14] H. A. Macleod, *Thin-Film Optical Filters*, Adam Hilger (Publishing Company), Techno House, Bristol, 1986.
- [15] M. H. Suhail, G. M. Rao, and S. Mohan, "dc reactive magnetron sputtering of titanium-structural and optical characterization of TiO_2 films," *J. Appl. Phys.* **71**, 1421-1427 (1992).

Chapter 7

Summary

The principle motivation of the present work was to explore the optical properties of bulk materials and thin films deposited on various substrates by using the spectroscopic ellipsometer. In this work, there were several different facets of the problem. These involved surface treatment of samples measured, selecting on of a suitable analysis model and requirement of much computational efforts. Here we summaries the salient features of this work.

In chapter 1, the background and purpose of this research, and main analysis method were described.

In chapter 2, we had dealt with the mathematical representations that are employed to describe polarized light, and we used these representations to discuss the interaction of polarized light with the optical components that may compose an ellipsometer. The mathematical tool are applied to analyze the theory of measurement in ellipsometer, including to give a relation between the SE parameters (Δ and Ψ) and the normalized Fourier coefficients (a_2 and b_2) of the rotating-analyzer system. On the reflection of polarized light by stratified planner structures is intended to provide results and techniques that are essential for the interpretation of ellipsometric data in terms of the macroscopic properties of particular sample under measurement. We have also described the Levenberg-Marquardt Method, which was widely applied to analyze SE data.

We place emphasis on our proposed analysis model (Modified Harmonic Oscillator Approximation Scheme for the Dielectric Constants of Semiconductor). The model presented

CHAPTER 7. Summary

here is mathematically simple, and related to the electronic energy-band structures of the medium. This model is applicable over the entire range of photon energies, below and above the lowest band gaps, and it exactly satisfies the Kramers-Kronig relations. It also requires the minimum number of parameters to yield excellent simultaneous fits to $\varepsilon_1(\omega)$ and $\varepsilon_2(\omega)$ and their first three numerical derivatives with respect to photon energy. The parameters of the model can be determined as functions of x for $\text{Al}_{1-x}\text{Ga}_x\text{As}$.

In chapter 3, the characterization results of a strained GaP layer grown on a Si substrate by spectroscopic ellipsometry have been described. The band-gap energies of GaP and Si, GaP layer thickness and the GaP oxide layer for a strained GaP/Si heterostructure were determined by the calculated fitting. The compressive stress applied to the GaP layer and the tensile stress applied to the Si substrate decrease gradually with increasing GaP layer thickness in the thickness range less than the critical thickness. The lattice relaxation of GaP occurs gradually with increasing thickness.

The MOCVD-grown GaAs on Si have been investigated by SE. The results obtained from the proposed model indicate that it can be simultaneously determined the thicknesses, stress and crystalline quality. The tensile stress is applied to GaAs layer and the GaAs on Si with AlGaP+SLS intermediate layer has best surface morphology and crystalline quality. Further, the surface morphology of NaOCl-polished GaAs grown on Si have been measured by SE and AFM. The maximum value of ε_2 ($\sim 4.77\text{eV}$) is 24.5 and typical rms is 0.3 nm. The depth of surface roughness determined by SE is in agreement with rms roughness obtained by AFM. Therefore, the surface roughness of GaAs on Si can be reduced to 1/10 that in the as-grown state using NaOCl-polishing, and the results of surface characterization by SE are consistent with AFM measurements.

In chapter 4, poly-Si thin films, obtained by the crystallization of α -Si by laser annealing have been studied. Smooth poly-Si films have been obtained by the implementation of two step irradiation technique, i.e., 344 mJ/cm^2 pulse followed by $250 - 276\text{ mJ/cm}^2$ laser energy pulse. A detailed analysis of the $\varepsilon(\omega)$ demonstrate that increase of laser energy lead to an increase of the crystalline fraction and the crystalline grain size. It has also been observed that the crystalline size saturates at 260 mJ/cm^2 laser energy. Also, poly-Si films

exhibit tensile stress.

An amorphous thin films of $\text{Si}_{1-x}\text{Ge}_x$ /Si alloys have been deposited on glass and single crystal Si substrates by ion beam sputtering, and the composition (x) is controlled by varying the area of silicon wafers placed on the germanium target. Upon XeCl excimer laser annealing, these films reveal polycrystalline nature by both X-ray and SE measurements. The composition (x) of $\text{Si}_{1-x}\text{Ge}_x$ /Si films, evaluated from the SE dielectric function $\epsilon(\omega)$ data using the second derivative technique, are in agreement with those obtained from X-ray and AES measurements within their experimental limitations.

It has also been observed that the (111) orientation is predominant in all of poly- $\text{Si}_{1-x}\text{Ge}_x$ /Si films on both the substrates. This dominant of (111) orientation is attributed to the free surface energy of films which plays a major role in the crystallization process. Furthermore, the detailed analysis of X-ray diffraction data and SE measurements show that the average microcrystallite size decreases with increasing Ge mole fraction, and the volume fraction of crystalline $\text{Si}_{1-x}\text{Ge}_x$ /Si increases with increasing laser irradiation energy. These phenomena have been attributed to different degree of annealing and hence the changing in the degree of crystallinity.

Finally, the optical gap of these films have been obtained in terms of E_{04} (defined as the energy at which α is equal to 10^4 cm^{-1}) from the absorption coefficient spectra and the value is found to be in the range of 1.05 - 1.28 eV for two Ge concentrations. These results further support to conclude that the $\text{Si}_{1-x}\text{Ge}_x$ /Si alloy provides continuously and widely variable optical band gap.

In chapter 5, using an accurate film thickness which can be obtained by SE, one can determine optical functions of GaN by both SE and transmission method leading to the same results in the common wavelength region. The free exciton absorption in high-quality GaN sample is evidently observed at room temperature, with the transition energy at about 3.44 eV. However, the deep level absorption near 2.0 eV is not observed.

The refractive indices n_{\perp} and n_{\parallel} as a function of wavelength over the wavelength range of 370 to 820 nm have obtained. The calculated spectra of the refractive indices n_{\perp} and n_{\parallel} are also analyzed using the first-order Sellmeier equation. The values of the high-frequency

CHAPTER 7. Summary

dielectric constant obtained are 5.14 for ($E \perp c$) and 5.31 for ($E \parallel c$). These values are close to the direct experimental observations (5.35).

Young's modulus of GaN film on sapphire substrate using the nano-indentation experiment have been estimated, and found that the maximum shear stress depends on the quality of the crystal. The maximum shear stress is 5.4 GPa for the high-quality GaN film. The "true-hardness" of GaN film is 53.6 GPa, which is larger than that of $\text{In}_{0.1}\text{Ga}_{0.9}\text{N}$ film on sapphire, and smaller than that of sapphire.

The optical constants of $\text{Al}_x\text{Ga}_{1-x}\text{N}$ can be accurately expressed as the sum of Sellmeier dispersion equation and a free exciton below the fundamental band edge. The free exciton energy of $\text{Al}_x\text{Ga}_{1-x}\text{N}$ has been obtained by simultaneously fitting to SE data Ψ measured at three angles of incidence, 40° , 50° and 60° . The values obtained vary from 3.44 to 3.95 eV when the composition x varies from 0 to 0.151.

In chapter 6, sol-gel derived TiO_2 thin films, both amorphous and nanocrystalline, are investigated for optical properties by spectroscopic ellipsometry and transmission spectroscopy. A method to fit simultaneously the measured parameters of SE, Ψ and Δ , for inhomogeneous thin film has also been described. Instead of the refractive index, volume fraction of void has been assumed to vary along the thickness of the film in the fitting analysis and an excellent fit has been obtained for both the amorphous and nanocrystalline TiO_2 films. Nearly linear refractive index gradient has been obtained for both the samples with sample 2 having a larger index gradient than sample 1 showing deterioration of homogeneity with increase in annealing temperature. The degree of inhomogeneity obtained are 5-6% and 12-14% for samples 1 and 2, respectively, and are higher than those reported for TiO_2 films deposited by EB evaporation (3 - 5 %) and rf sputtering (5 %) techniques. Extinction coefficients $k(\lambda)$ of the samples are calculated from the transmission spectra. Nonzero k values for sample 2 at photon energies much lower than the fundamental band gap energy (3.2 eV) show scattering effect in the nanocrystalline TiO_2 film.